Wavelet-based wavenumber spectral estimate of eddy kinetic energy: Application to the North Atlantic

Takaya Uchida, COAPS (tuchida@fsu.edu)
Quentin Jamet, INRIA (quentin.jamet@inria.fr)
Andrew Poje, CUNY (andrewpoje@gmail.com)
Nico Wienders, FSU (wienders@fsu.edu)
William K. Dewar, FSU (wdewar@fsu.edu)

Wavelet-based wavenumber spectral estimate of eddy kinetic energy: Application to the North Atlantic

Takaya Uchida[1,2], Quentin Jamet[2,3], Andrew C. Poje[4], Nico Wienders[5]& William K. Dewar[2,5]

[1]Center for Ocean-Atmospheric Prediction Studies, Florida State University, Florida, USA
[2]Université Grenoble Alpes, CNRS, INRAE, IRD, Grenoble-INP, Institut des Géosciences de l'Environnement, Grenoble, France
[3]INRIA, ODYSSEY group, Ifremer, Plouzané, France
[4]Department of Mathematics, College of Staten Island, The City University of New York, New York, USA
[5]Department of Earth, Ocean and Atmospheric Science, Florida State University, Florida, USA

Key Points:

- Wavenumber spectra of eddies, defined as the fluctuations about an ensemble mean, are estimated for the North Atlantic basin.
- The wavenumber spectra and spectral flux of eddy kinetic energy and enstrophy are estimated using wavelet transform.
- We question the validity of quasi-geostrophic thinking for spectral slopes and offer a primitive equation extension.

Corresponding author: William K. Dewar, `wdewar@fsu.edu`

Abstract

An ensemble of eddy-rich North Atlantic simulations is analyzed, providing estimates of kinetic energy wavenumber spectra and spectral budgets below the mixed layer where energy input from surface convection is negligible. A wavelet transform technique is used to estimate a localized 'pseudo-Fourier' spectrum, permitting comparisons to be made between spectra at different locations in a highly inhomogeneous and anisotropic environment. We find evidence of a Gulf Stream imprint on the near Gulf Stream eddy field appearing as enhanced levels of kinetic energy (KE) in the North-South direction relative to the East-West direction. Surprisingly, this signature of anisotropy holds into the quiescent interior. We detect forward cascades of KE and enstrophy but find no clear evidence of upscale energy cascades in the separated Gulf Stream region, although an inverse cascade of KE emerges downstream of the separated Gulf Stream. The spectral slopes inferred from our analysis are significantly steeper than expected from quasi-geostrophic (QG) theory, but roughly in line with a primitive equation extension of the enstrophy inertial-range theory. A summary conclusion is that expectations regarding spectral slopes built on quasi-geostrophy are at best only weakly supported in primitive equations below the mixed layer where submesoscale dynamics are expected to be weak.

Plain language summary

Describing the statistical characteristics of the weather system of the ocean, known as eddies, has been a long standing problem in the field of ocean science. This has been motivated by the fact that eddies contribute significantly to the global heat and carbon transport. Here, in analysing numerical simulations of the North Atlantic that partially resolve the eddies, we apply a relatively novel diagnostic framework based on wavelet functions to characterize the statistical nature of eddies in a realistic setting of the ocean. We find that the signature of the Gulf Stream imprints itself onto the eddy statistics.

1 Introduction

The ocean is 'turbulent', implying the presence of energetic and widespread spatial and temporal 'eddies' (Stammer, 1998; Stammer & Wunsch, 1999). It is now commonly accepted in ocean modeling that resolving these features, at least at the mesoscale, leads to ocean simulations of a much more realistic nature (Chassignet & Marshall, 2008; Chassignet et al., 2020; Griffies et al., 2015; Constantinou & Hogg, 2021; G. Xu et al., 2022), which may have important implications for climate projections (Saba et al., 2016; Beech et al., 2022). This implies the eddy field is an integral part of the ocean structure, and necessary to include in some fashion if acceptable ocean models are to be constructed. The computational demands of eddy-resolving resolution have led to the search for eddy parameterizations that faithfully capture the dynamical role of eddies in the absence of their explicit presence (e.g. Redi, 1982; Gent & Mcwilliams, 1990; Gent, 2011; Jansen et al., 2019; Guillaumin & Zanna, 2021; Berloff et al., 2021; Uchida, Deremble, & Popinet, 2022; Li et al., 2023, and references therein). It is essential therefore to understand the behavior of the eddy field in well-resolved models in order to ascertain the character eddy parameterizations should portray and to provide benchmarks for assessing the affects of any particular proposed parameterization. This paper attempts to serve these purposes by describing and applying a methodology that allows for spatial inhomogeneity in the mean flow to influence eddy characteristics. We analyze a recently developed ensemble of North Atlantic simulations (Jamet et al., 2019) and use two-dimensional wavelet analysis to diagnose the spectral structure.

Most available theoretical guidance on oceanic turbulence comes from quasi-geostrophic (QG) theory, where the combined conservations of energy and potential vorticity (PV) lead to predictions for specific shapes for wavenumber spectra. Surface quasi geostropy (SQG), on the other hand, employs conservation of surface buoyancy instead of PV (Held et al., 1995; Lapeyre, 2017). It is generally thought that the eddy field should display a so-called '$-5/3$' spectral slope as a result of an up-scale cascade of energy, and a '-3' slope due to a down-scale enstrophy cascade (Charney, 1971). Both predictions are based on the ideas of inertial ranges and involve a reasonable number of assumptions. Locality in spectral interactions, stationarity in time and homogeneity in space are amongst the most prominent assumptions; a thorough discussion appears in Vallis (2006). Numerical, observational and laboratory investigations in relevant settings tend to support the predictions (e.g. Gage & Nastrom, 1986; Yarom et al., 2013; Callies & Ferrari, 2013; Campagne et al., 2014).

The inertial-range ideas are usually adopted when venturing into the more dynamically complex settings of primitive equations and realistic ocean simulations (e.g. Y. Xu & Fu, 2011, 2012; Khatri et al., 2018; Vergara et al., 2019), although it is difficult to justify many of the assumptions. In particular, as will often be the focus of this paper, the presence of the Gulf Stream would seem to clearly violate spatial homogeneity in the field in which the eddies are viewed. In addition, and perhaps at an even more fundamental level, the mix of a coherent, large-scale mean with an incoherent, variable component renders the definition of what constitutes an 'eddy' somewhat vague. One then questions what features should be focused on when constructing a spectrum (cf. Uchida, Jamet, et al., 2021). This problem of identifying or defining ocean eddies is a well known one, with an early reference being Wunsch (1981).

Another problem facing the quantification of the eddy field in an inhomogeneous setting is a lack of available techniques for analyzing the data. A favorite, and classical, method for studying wavenumber spectra employs Fourier transforming momentum (e.g. Capet et al., 2008; Callies & Ferrari, 2013; Rocha et al., 2016; Uchida et al., 2017, 2019; Khatri et al., 2018, 2021). The connection between this measure and kinetic energy (KE) comes from Parseval's theorem, which equates the area integrated KE to the wavenumber integrated spectrum

$$\int_{\boldsymbol{x}} |\boldsymbol{u}(\boldsymbol{x})|^2 \, d\boldsymbol{x} = \int_{\boldsymbol{k}} \hat{\boldsymbol{u}} \cdot \hat{\boldsymbol{u}}^* \, d\boldsymbol{k} \tag{1}$$

where $\hat{\boldsymbol{u}}$ is the Fourier transform of $\boldsymbol{u} = (u, v)$. This permits the interpretation of the spectrum in terms of a wavenumber dependent energy density. However, this same equivalence then implies the resultant spectra are averages over the domain involved in the analysis. While this does not represent a conceptual problem if the domain is spatially homogeneous, the relation of the result to the local spectrum in an inhomogeneous setting is not clear.

Our primary numerical tool to tackle these questions is a recently developed eddying ensemble of partially air-sea coupled North Atlantic simulations. These simulations have been used before in studies of North Atlantic energetics (Jamet et al., 2020), the Atlantic Meridional Overturning Circulation (AMOC; Jamet et al., 2019; Dewar et al., 2022), Empirical Orthogonal Function (EOF) analyses of eddies (Uchida, Jamet, et al., 2021), and the thickness-weighted averaged (TWA) feedback of the eddies on the residual-mean flow (Uchida, Jamet, et al., 2022; Uchida, Balwada, et al., 2023). A full description of the simulations appears in Jamet et al. (2019). For our purposes, the ensemble consists of 48 members exposed to *small* initial-condition uncertainties (usually referred to as *micro* initial conditions; Stainforth et al., 2007) run at an 'eddy-rich' 1/12° resolution. A map of the surface eddy Ertel's PV appears in Fig. 1, displaying the expected activity around the Gulf Stream region, with a separation from the coastal U.S. around

Cape Hatteras, and North Atlantic Current. Also shown are six marked locations which will be referred to later in the text.

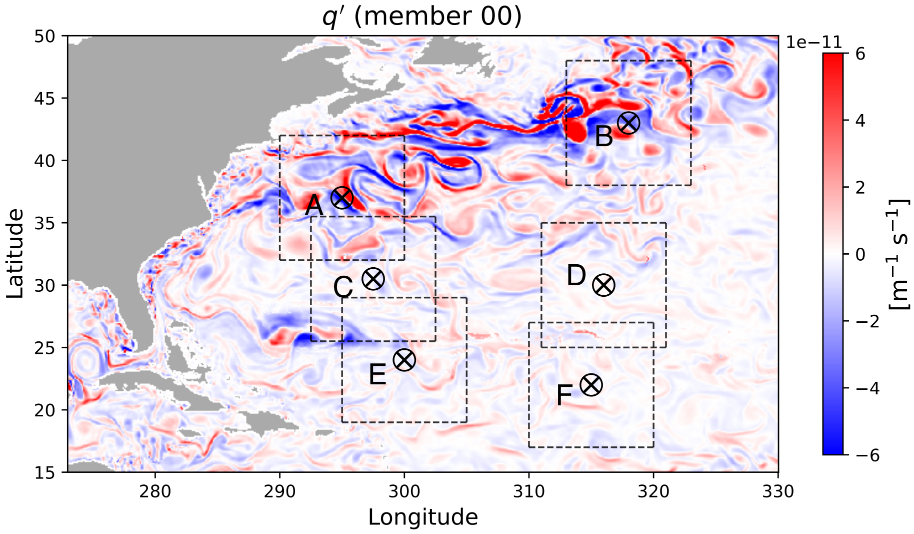

Figure 1. Surface eddy Ertel's PV from member 00 amongst the 48 ensemble members at 00:10, January 1, 1967 where buoyancy is defined as $\hat{b} = -\delta/\rho_0$ and is dimensionless (cf. Section 3.1.4 and Appendix A). Land and coastlines are in grey; the Gulf Stream and its extension into the open Atlantic are visible. Locations within the Gulf Stream near to separation at Cape Hatteras and North Atlantic Current are marked, as are other locations in the North Atlantic interior and gyre retroflection with six regions in total named from A to F. The dashed lines indicate the $10^\circ \times 10^\circ$ domains over which the wavelet transforms are applied. These locations will be referred to later in the text.

We assert that such an ensemble leads to a clear identification of oceanic eddies, namely as fluctuations about the ensemble mean. Specifically, we can average our simulations at any space and time point across our ensembles to obtain an estimate of the classical ensemble mean. Then, we can revisit each individual ensemble member to compute its deviation from the ensemble mean at that same spatial and temporal location. Inasmuch as the ensemble mean represents that component of the solution common to all members, we identify it as the predictable part of the flow. The residuals, belonging to each individual realization, are the 'unpredictable' components of the flow and are identified as the eddies. An attempt to rationalise this in terms of integrated KE budgets has recently been proposed by Jamet et al. (2022). Note that this eddy definition is independent of any arbitrarily chosen spatial or temporal scale, a highly desirable feature not characteristic of most definitions reliant on some form of spatial or temporal filtering (Chen & Flierl, 2015; Uchida, Deremble, Dewar, & Penduff, 2021; Uchida, Jamet, et al., 2021; Berloff et al., 2021). These eddies are the ones we propose to quantify.

As to spectral computations, we proceed using a wavelet-based analysis. To our knowledge, the wavelet approach to wavenumber spectra was initially examined by Daubechies (1992) and Perrier et al. (1995) and in an oceanographic context by Uchida, Jamet, et al. (2023). For our purposes, we will interpret the spectra computed using wavelets as an estimate of a localized 'pseudo-Fourier' spectrum, which is backed by the Parseval's equality (Uchida, Jamet, et al., 2023). The locality of these estimates permits us to examine and compare the variability of the spectra throughout the domain.

Our eddy definition is reviewed briefly in the next section, along with a description of our wavelet-based analysis methods. Section 3 presents a comparison between wavelet-based spectral estimates and the canonical Fourier-based estimates within the North Atlantic gyre. The paper ends with a Discussion, speculations on the relevant dynamics and plans for further work.

2 Theory and techniques

In this section, we describe our definition of 'eddies' (Section 2.1) and provide an overview on wavelet analysis (Section 2.2).

2.1 Eddy Definition

Due to the chaotic nature of the ocean (Poincaré, 1890; Lorenz, 1963), trajectories of eddying numerical simulations are sensitive to initial condition uncertainties (e.g. Kay et al., 2015; Sérazin et al., 2017; Maher et al., 2019; Zhao et al., 2021; Uchida, Deremble, & Penduff, 2021; Leroux et al., 2018, 2022; Jamet et al., 2022; Germe et al., 2022; Romanou et al., 2023). This allows us to develop an ensemble of ocean simulations, differing only in small ways in their initial conditions; i.e. simulations based on initial states that have small differences well within current measurement uncertainties. It is a matter of experience that while gross characteristics of the resulting fully evolved states are similar (there will always be a Gulf Stream, for example), the mesoscale fields become incoherent. While each ensemble solution represents an equally valid and plausible simulation of the North Atlantic, none of them at any specified date will recreate the observed ocean state since the observed ocean is itself a single realization of the chaotic system.

From such an ensemble, one can take an 'ensemble mean', which we will denote by brackets, i.e. for any model variable $\psi(\boldsymbol{x},t)$,

$$\langle \psi(\boldsymbol{x},t) \rangle = \frac{1}{N} \sum_{i=1}^{N} \psi^i(\boldsymbol{x},t) \, , \tag{2}$$

where N is the total number of ensemble members and the superscript i denotes the ensemble member. We interpret the ensemble mean as the 'forced' response of the ocean. That is, as the ensemble mean is common to all members, it reflects the common external conditions imposed at the boundaries of the system. In our case, these common conditions consist of the prescribed atmospheric states and the open ocean boundary conditions at the northern and southern domain boundaries and the Strait of Gibraltor (Jamet et al., 2019).

The eddy field is denoted by deviations of ψ about the ensemble mean

$$\psi^{i\prime}(\boldsymbol{x},t) = \psi^i(\boldsymbol{x},t) - \langle \psi(\boldsymbol{x},t) \rangle \, . \tag{3}$$

Each member, i, having its own eddy field thus identifies the eddies as an unpredictable component of the flow. Note that the ensemble mean in (2) is inherently a function of space and time, a feature which permits the examination of the non-stationary and inhomogeneous character of the statistics. It is a strength of the ensemble dimension, being orthogonal to the space-time dimensions, that these features of non-stationarity and inhomogeneity are preserved.

Finally, we note that the ensemble mean structure of the ocean is not independent of the eddies, rather the equations of motion in their non-linearity involve higher-order measures of the eddies as part of their balance. Each realization, in turn, is constrained by the lower-order statistics of the eddy contributions.

2.2 Spectral Considerations

We depart from the classical Fourier approach to compute wavenumber spectra for our non-periodic and inhomogenous settings, but do note the utility of wavenumber spectrum emerges largely from Parseval's equality (cf. Uchida, Jamet, et al., 2023, their Appendix A). We base our spectral analysis on wavelet decompositions. Here, we provide a brief overview.

Given a function of two spatial dimensions, $f(\boldsymbol{x})$, its continuous wavelet transform is given by

$$\tilde{f}(s,\phi,\boldsymbol{\gamma}) = \int_{\boldsymbol{x}} f(\boldsymbol{x})\frac{1}{s}\xi^*(\mathsf{R}^{-1}\cdot\left(\frac{\boldsymbol{x}-\boldsymbol{\gamma}}{s}\right))\,d\boldsymbol{x}\,, \tag{4}$$

where R^{-1} is the inverse of the rotation matrix

$$\mathsf{R}^{-1} = \begin{pmatrix} \cos(\phi) & \sin(\phi) \\ -\sin(\phi) & \cos(\phi) \end{pmatrix}\,, \tag{5}$$

for rotation through an angle ϕ. The quantity s is referred to as the 'scale', $\boldsymbol{\gamma}\,(\in \mathbf{R}^2)$ is the two-dimensional coordinates of interest, $\xi(\boldsymbol{x})$ is the so-called 'mother' wavelet and $\xi(\mathsf{R}^{-1}\cdot(\boldsymbol{x}-\boldsymbol{\gamma})\,/s)$ in (4) are the daughter wavelets. The quantities $\tilde{f}$ are the wavelet coefficients. Subject to a few, relatively easy to meet conditions (Uchida, Jamet, et al., 2023), the original data can be reconstructed from the wavelet coefficients via an inverse wavelet transform

$$f(\boldsymbol{x}) = \mathscr{C}\int_{\boldsymbol{\gamma}}\int_{\phi}\int_{s}\frac{1}{s^4}\tilde{f}(s,\phi,\boldsymbol{\gamma})\xi(\mathsf{R}^{-1}\cdot\left(\frac{\boldsymbol{x}-\boldsymbol{\gamma}}{s}\right))\,ds\,d\phi\,d\boldsymbol{\gamma} \tag{6}$$

where $\mathscr{C}$ is a constant, to be clarified below. Exploiting the properties of wavelets, it is possible to show they satisfy a generalized Parseval's equality

$$\int_{\boldsymbol{x}} f(\boldsymbol{x})g(\boldsymbol{x})d\boldsymbol{x} = \mathscr{C}\int_{\boldsymbol{\gamma}}\int_{\phi}\int_{s}\frac{\tilde{f}\tilde{g}^*}{s^3}\,ds\,d\phi\,d\boldsymbol{\gamma}, \tag{7}$$

with $\bullet^*$ the complex conjugate. Note, if $f = g$, (7) corresponds to the Parseval's equality in (1).

We employ the so-called Morlet wavelet (Morlet et al., 1982; Gabor, 1946), i.e.

$$\xi(\boldsymbol{x}) = \left(e^{-2\pi i\boldsymbol{k}_0\cdot\boldsymbol{x}} - c_0\right)e^{-\frac{\boldsymbol{x}\cdot\boldsymbol{x}}{2x_0^2}}\,, \tag{8}$$

where c_0 is a constant included to insure that the wavelet has zero mean $\int_{\boldsymbol{x}}\xi(\boldsymbol{x})d\boldsymbol{x} = 0$. The central wavenumber $\boldsymbol{k}_0$ is taken to be $\boldsymbol{k}_0 = (k_0, 0)$ and the quantity x_0 is a reference length scale, here taken to be 50 km, viz. the length scale of the mother wavelet. The zonal orientation of wavevector $\boldsymbol{k}_0$ is arbitrary as we will rotate the orientation with R. We will choose $k_0 = 1/x_0$, in which case the constant c_0 is quite small and generally ignored (i.e. $c_0 = 0$), a convention adopted in this paper. Plots of (8) are found in Fig. 2. Note that the Morlet mother wavelet consists of a wave of wavelength $L = x_0$ inside a Gaussian envelope of decay scale $\sqrt{2}x_0$. Thus for $s = 1$ and $\phi = 0$, the wavelet coefficient produced by this transformation comments on the presence of the wavenumber $\boldsymbol{k}_0 = (k_0, 0)$ at location $\boldsymbol{\gamma}$ in the original data. Increasing the rotation angle ϕ and filtering returns information about the presence of the same wavelength at angle ϕ. Finally allowing s to vary modifies the filter so that the primary wavelength of the filter is $k = 1/(sx_0)$. The Morlet wavelet coefficient can thus be thought of as a 'local' Fourier transform at wavenumber $\boldsymbol{k}_0^\intercal \cdot \mathbf{R}^{-1}(\phi)/s$, where the superscript $\intercal$ denotes a transpose.

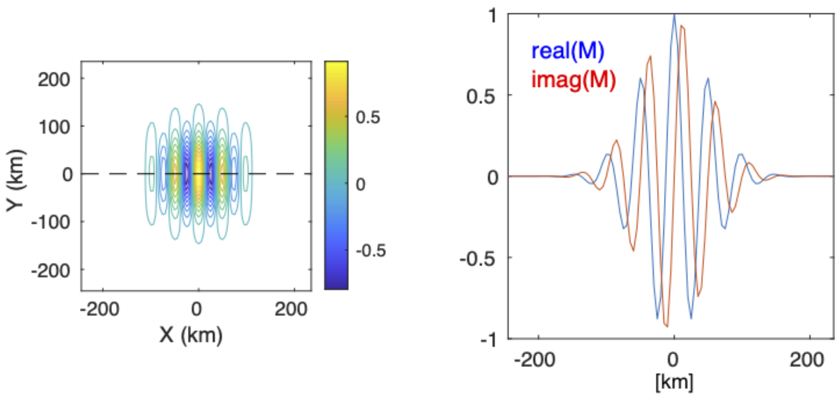

Figure 2. Structure of the Morlet wavelet with the reference length scale $x_0 = 50\,\mathrm{km}$. A contour plot of the real part of the mother Morlet wavelet is shown in the left panel. Transects of the real and imaginary parts along the dashed line appear in the right panel.

At this point, the scale factor in (4), s, is non-dimensional. It is more traditional in oceanography to discuss energy spectra in terms of wavenumber. As pointed out above, the effective wavenumber associated with s is $k = 1/(sx_0) = 1/s_0$, where the quantity s_0 has units of length. Upon some algebra, one may transform (7) (with $f = g$) to wavenumber, $k = 1/s_0$, space, ending with

$$\int_{\boldsymbol{x}} f^2(\boldsymbol{x}) d\boldsymbol{x} = \frac{1}{C_\Xi} \int_\phi \int_k \int_\gamma \tilde{f}^* \tilde{f} k x_0^2 \, d\gamma \, dk \, d\phi \,, \tag{9}$$

where $C_\Xi = \int_{\boldsymbol{k}} \frac{\hat{\Xi}^* \hat{\Xi}}{\boldsymbol{k} \cdot \boldsymbol{k}} \, d\boldsymbol{k}$ and $\hat{\Xi}$ is the Fourier transform of the mother wavelet (cf. Uchida, Jamet, et al., 2023). Note, $\mathscr{C} = C_\Xi^{-1}$ in (7).

If we now produce wavelet coefficients for the zonal and meridional eddy velocities u'^i and v'^i from member i of our ensemble, and manipulate them appropriately, we obtain

$$\widetilde{E}_K^i(\gamma, \phi, k) = \frac{1}{C_\Xi} \frac{\widetilde{u'^i} \widetilde{u'^i}^* + \widetilde{v'^i} \widetilde{v'^i}^*}{2} x_0^2 k \,, \tag{10}$$

as a measure of energy density in wavelet transform space. Each value of $\widetilde{E}_K^i$ is a random number as each ensemble member possesses a 'random' eddy field emerging from the non-linearities in the system. Ensemble averaging those values returns an estimate of the ensemble-mean energy spectrum as a function of wavenumber k in direction ϕ. The spatial locality of the mother wavelet permits the interpretation of $\widetilde{E}_K(s,\phi,\boldsymbol{\gamma}) = \langle \widetilde{E}^i_K(s,\phi,\boldsymbol{\gamma})\rangle$ as the local energy spectrum at location $\boldsymbol{\gamma}$.

In calculating the wavelet coefficients, we spatially interpolate each $10^\circ\times10^\circ$ domain centered around each $\otimes$ in Fig. 1 onto a uniform grid (cf. section 3). The wavelet transform appropriate to the scale factor s was then taken between $[k_F^{\min}, k_F^{\max}]$ with 40 monotonic increments where $k_F^{\min}$ and $k_F^{\max}$ are the minimum and maximum Fourier wavenumbers respectively leaving us with 47 increments, and angle ϕ with the resolution of $\pi/18$ radian ($= 10^\circ$) between $[0,\pi)$. The scaling was then truncated at scales below 50 km and appended with scales corresponding to the Fourier wavenumbers to increase the wavenumber resolution at higher wavenumbers. The spatial integration of the product of the wavelet and the data is the wavelet coefficient for each location.

3 Results

In this section, we examine the kinetic energy (KE) and enstrophy spectra and spectral flux from the various locations in Fig. 1; the location of the panels correspond to the locations on the map. We remind the reader that enstrophy here is defined by Ertel's potential vorticity (PV). The depth of 452 m was chosen to be within the general wind-driven circulation but well beneath the mixed layer in order to avoid KE input from convective events (cf. Uchida, Jamet, et al., 2022, their Fig. 2b), in our case parametrized by the K-profile parametrization (KPP; Large et al., 1994). The 48-member ensemble outputs used in this study are instantaneous snapshots at 00:10, January 1, 1967. No temporal averaging has been applied. By this date, four years after the initial ensemble generation, ensemble statistics have saturated. Similar spectral analyses at location A, performed on the same date at 10-year intervals in the available 50 years of five-day averaged outputs (not shown) produce statistically equivalent results.

Prior to taking the wavelet transforms, the fields were linearly interpolated onto a uniform grid. In order to account for the finite-volume discretization of MITgcm, we first weighted the velocity fields by the grid area. The velocities were then linearly interpolated onto the uniform grid and divided by the area also interpolated onto the uniform grid. The uniform grid spacings were taken as the minimum spacing per $10^\circ\times10^\circ$

domain centered around each location in Fig. 1. The wavelet transforms are taken at the center of the $10° \times 10°$ domain while the Fourier transforms are taken over the $10° \times 10°$ domain.

3.1 The wavelet and Fourier approach

One of the major differences between quasi geostrophy and primitive equations is that advection is two-dimensional (2D) in the former and three-dimensional (3D) for the latter. It can be argued that for primitive equations, the eddy velocity defined about the thickness-weighted averaged residual mean, which reduces to 2D under adiabatic conditions (Young, 2012; Marshall et al., 2012; Aoki, 2014; Loose et al., 2022; Uchida, Balwada, et al., 2023; Meunier et al., 2023), corresponds to the QG eddy velocities under order-Rossby number fluctuations in the layer thickness. Nonetheless, the spectral flux of KE and enstrophy have commonly been examined in geopotential coordinates (e.g. Capet et al., 2008; Arbic et al., 2013; Khatri et al., 2018, 2021; Ajayi et al., 2021). Due to the discrepancies between quasi geostrophy and primitive equations in geopotential coordinates, there is no guarantee that the inertial-range theory should hold for the latter. In this section, we examine the agreement between the wavelet and Fourier approach, and to what extent the spectra and spectral fluxes in geopotential coordinates are consistent with QG predictions. We also include contributions from vertical advection unlike studies using satellite observations where only the horizontal velocities are available (Scott & Wang, 2005).

3.1.1 Spectral Estimates

We start by comparing the wavenumber spectra derived from wavelet and traditional Fourier methods at Location A. Prior to taking the Fourier transform, land cells surrounded by ocean were linearly interpolated over and filled in with zeros otherwise. A standard Hann window was then applied to make the data doubly periodic. To conduct a direct comparison of the two methods, land cells are similarly treated before performing the wavelet analysis, which requires no windowing. In all cases, bootstrapped confidence intervals are provided by randomly resampling (with replacement) from the 48 ensemble member energy densities 9999 times.

As shown in Fig. 3a, the two approaches agree well in their spectral estimates. Such a similarity between Fourier and wavelet estimates have also been identified in doubly periodic homogeneous QG simulations where Fourier modes are best suited (Uchida, Jamet, et al., 2023). The overall spectral slopes are relatively steep. A best fit to the spectra between roughly 250 km and 40 km suggests a -4.13 power law, which is considerably steeper than either the $-5/3$ or -3 energy and enstrophy inertial range laws emerging from standard scaling analysis of quasi geostrophy.

We have also computed the spectra of Ertel's PV spectra at this location and depth (Fig. 3c). Again, standard Fourier and wavelet estimates agree within confidence bars. Consistent with the observations of steep KE spectra, the PV spectral slopes are considerably steeper than -1 (shown by the dashed line) expected from QG scaling in a forward enstrophy cascade.

3.1.2 Spectral Budgets

In the ocean, it is unlikely that the sources and sinks of energy are localized in wavenumber as assumed by standard, idealized inertial-range theories. Estimates of the scale-dependence can be made by explicitly computing wavelet-tranforms of the 'dynamics', i.e. transforms of all the terms in the eddy KE spectral budget

$$T_K = P_K + A_K + \mathrm{MtE}_K + \mathcal{K}_K \tag{11}$$

where the tendency of KE, T_K, equals the sum of pressure work P_K, advection A_K, KE exchange with the mean flow MtE_K, and non-conservative terms $\mathcal{K}_K$ respectively. Detailed notations of each term are given in (B6). Our form of pressure work consists only of the wavelet transforms related to $-\langle \boldsymbol{u}' \cdot \nabla_{\mathrm{h}} \phi' \rangle$. Adding and subtracting $\langle w'b' \rangle$ and using the hydrostatic relationship demonstrates that exchanges between potential and kinetic energies are contained in this term. We do not consider potential energy explicitly here, leaving this as a topic for consideration elsewhere.

The relative contributions of terms in the spectral budget computed at location A are shown in Fig. 3b where the residual (grey dashed line) is seen to be negligible. Namely, we are able to spectrally close the KE budget with wavelets, exemplifying their utility. Positive values indicate a source for the eddy KE reservoir and negative values a sink at a given wavenumber. The largest values from the dynamics belong to pressure work, KE tendency and advection. However, all the quantities, except for advection, are not distinguishable from zero at the 95% confidence level. The non-conservative term is expected to be very small as we are below the mixed layer. The advection A_K is positive across all wavenumbers, which would imply a forward cascade of energy. The levels of kinetic energy exchange with the mean flow are quite low, and insignificant (green curve in Fig. 3b). The pressure work term, while noisy, tends to peak at around 250 km (red curve in Fig. 3b), so QG theory might argue for an upscale energy cascade at smaller wavenumbers (Vallis, 2006). This is not what we find (i.e. $A_K > 0$), however, arguing for a deviation from quasi geostrophy in our results.

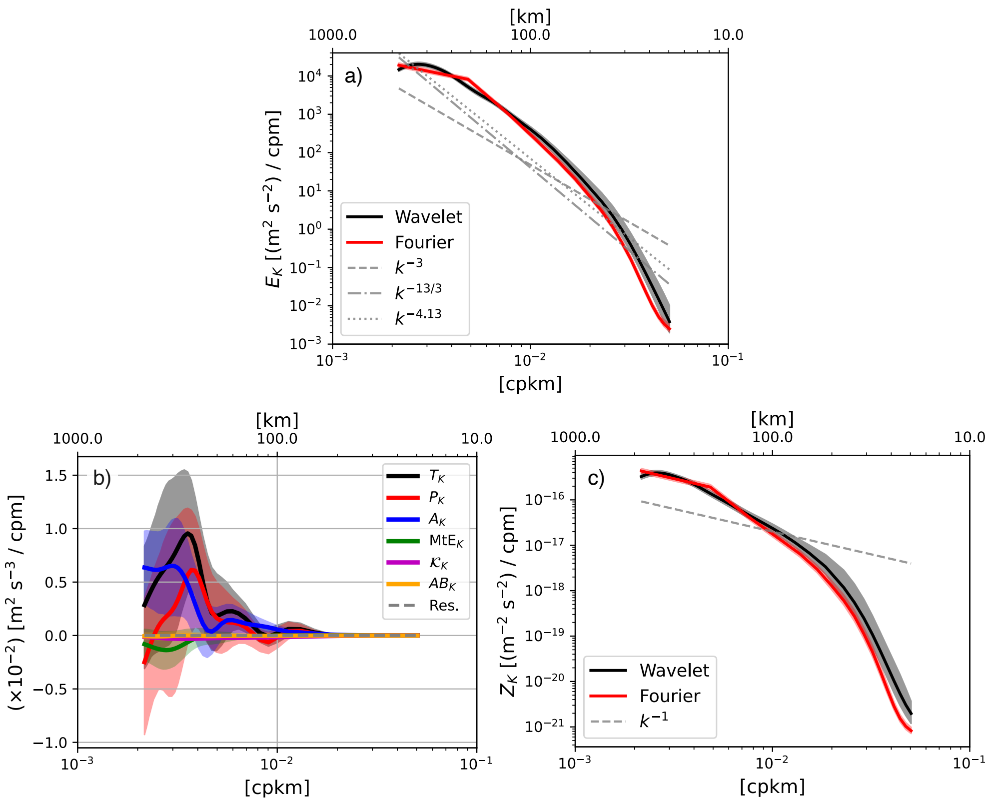

Figure 3. Isotropic (azimuthally-integrated) KE spectrum $E_K(k)$ using the wavelet and Fourier approach from $z = -452$ m at location A (indicated in Fig. 1) shown as black and red curves respectively on January 1, 1967 (a). The isotropic wavelet spectral KE budget (B6) is shown in panel (b) with the AB$_K$ term stemming from the Adam-Bashforth time stepping. The residual in the spectral budget is shown as the grey dashed curve being negligible. The isotropic enstrophy spectrum $Z_K(k)$ where buoyancy is dimensionless (cf. Section 3.1.4) (c). The land cells are interpolated over except for the budget. The colored shadings indicate the 95% bootstrap confidence interval.

The temporal stability of these results can be assessed by conducting the same analysis on data five and 10 days later in time. The lack of significance for most of the sizeable quantities, like pressure work and kinetic energy tendency manifest in greatly different values for these quantities on those dates. Clearly, they are not stable in sign (Fig. 4). In contrast, advection is persistently positive and significant at the 95% level and scales above $\sim 300\,\mathrm{km}$ at point A. T_K largely fluctuates with P_K. Namely, the pressure work is largely passed onto the tendency term, which might suggest signals propagating through location A from its surroundings. As the ensemble mean, which captures the oceanic response to atmospheric forcing, is removed from the spectral calculations, the signals are likely due to oceanic intrinsic variability including mesoscale eddies.

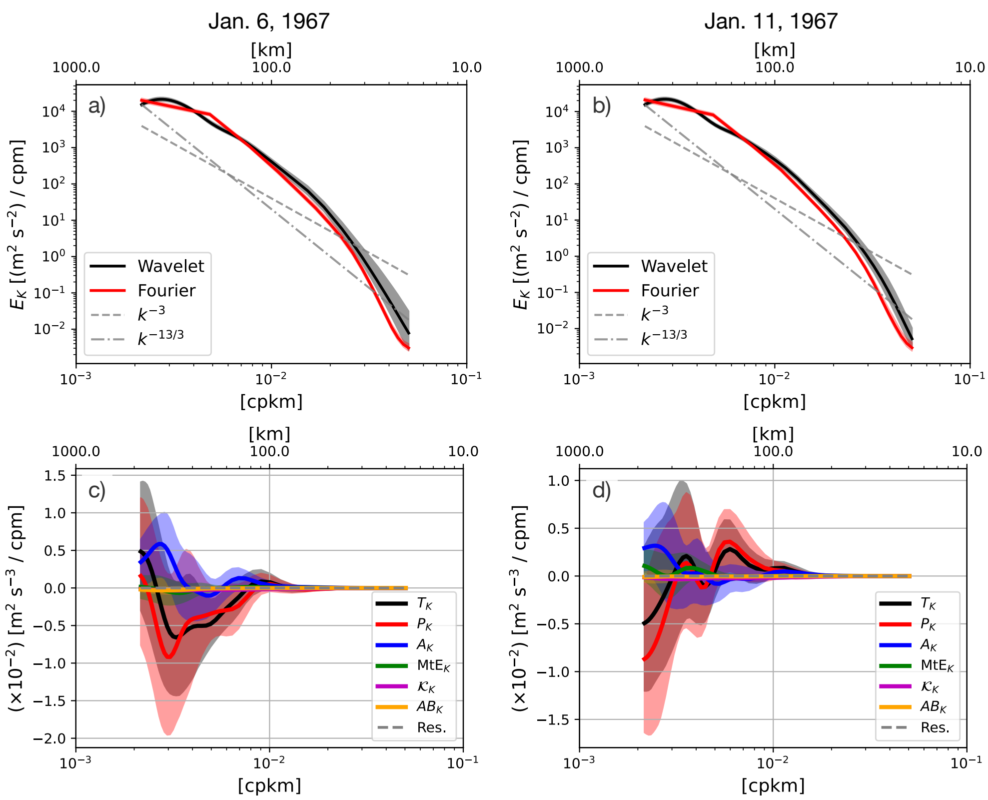

Figure 4. The KE spectra and spectral budget at location A on January 6 and 11, 1967 from $z = -452\,\mathrm{m}$. The land cells are interpolated over for the spectra to make the Fourier and wavelet approach consistent with each other but are not interpolated for the budgets.

3.1.3 Spectral Fluxes

Using the wavelet transforms, we can also diagnose the KE and enstropy spectral flux given respectively as

$$\tilde{\varepsilon}_K(\boldsymbol{\gamma}, \phi, k) = -\frac{1}{C_\Xi} \int_{k>\kappa} \mathcal{R}\left[\langle \tilde{u'}^* (\widetilde{\boldsymbol{v} \cdot \nabla u})' \rangle + \langle \tilde{v'}^* (\widetilde{\boldsymbol{v} \cdot \nabla v})' \rangle + \widetilde{\langle u \rangle}^* \nabla \cdot \widetilde{\langle \boldsymbol{v}' u' \rangle} + \widetilde{\langle v \rangle}^* \nabla \cdot \widetilde{\langle \boldsymbol{v}' v' \rangle} \right] x_0^2 \kappa \, d\kappa \,, \tag{12}$$

$$\tilde{\eta}_K(\boldsymbol{\gamma}, \phi, k) = -\frac{1}{C_\Xi} \int_{k>\kappa} \mathcal{R}\left[\langle \tilde{q'}^* (\widetilde{\boldsymbol{v} \cdot \nabla q})' \rangle + \widetilde{\langle q \rangle}^* \nabla \cdot \widetilde{\langle \boldsymbol{v}' q' \rangle} \right] x_0^2 \kappa \, d\kappa \,, \tag{13}$$

where $\mathcal{R}[\cdot]$ indicates the real part and κ is a dummy variable (Appendix B). Positive values indicate a forward cascade towards smaller scales and negative values an inverse cascade towards larger scales. The Fourier equivalent of $\langle \tilde{\boldsymbol{u}'}^* \cdot (\widetilde{\boldsymbol{v} \cdot \nabla \boldsymbol{u}'}) \rangle$, which is implicitly included in (12), corresponds to the KE spectral fluxes often examined by others (note whether the $'$ is inside or outside the round brackets). While the scale transfer of total KE is unequivocally captured by $\langle \boldsymbol{u} \cdot (\boldsymbol{v} \cdot \nabla \boldsymbol{u}) \rangle$, as geostrophic turbulence alludes to 'eddies', we have decomposed the flow into its mean flow and eddies. As a result, the additional non-local term related to $\langle \boldsymbol{v}' \cdot \nabla(\langle \boldsymbol{u} \rangle \cdot \boldsymbol{u}') \rangle$ emerges in the scale transfer term (cf. (B5)). In analogy to quasi geostrophy, one could make the claim that the corresponding term of KE scale transfer for the eddies in primitive equations should be $\langle \tilde{\boldsymbol{u}'}^* \cdot (\widetilde{\boldsymbol{v} \cdot \nabla \boldsymbol{u}'}) \rangle$ but based on (B5), we argue that the spectral flux should include the non-local term precisely because it can be incorporated as a divergence term. Jamet et al. (2022) has exhibited that the non-local transfer has leading-order importance in the KE budget. In the classical QG inertial-range theory, there is no presence of a mean flow ($\langle \boldsymbol{u} \rangle = \boldsymbol{0}$), so the non-local term does not emerge (Uchida, Jamet, et al., 2023).

The azimuthally-integrated spectral fluxes of KE and PV are shown for both the Fourier and wavelet approaches in (Fig. 5). While there is general agreement between the two estimates (within 95% confidence intervals), the wavelet approach provides freedom of scale selection and the elimination of windowing effects thus reducing flux uncertainty at the largest scales.

Both approaches indicate a forward energy flux at all available scales, but neither indicate the existence of an inertial range where the energy-flux might be considered scale independent. In contrast, the wavelet based estimate of the isotropic spectral flux of Ertel's enstrophy is relatively constant, and positive across the large scales, albeit with sizeable uncertainties. As in the KE flux, the wavelet approach shows reduced uncertainty at the largest scales where the Fourier flux is likely affected by the windowing (cf. Uchida, Jamet, et al., 2023). The entropy spectral flux remains relatively constant over a range of wavenumbers also on January 6 and 11, 1967 compared to the KE flux, which varies widely over wavenumbers (Fig. 5c,d).

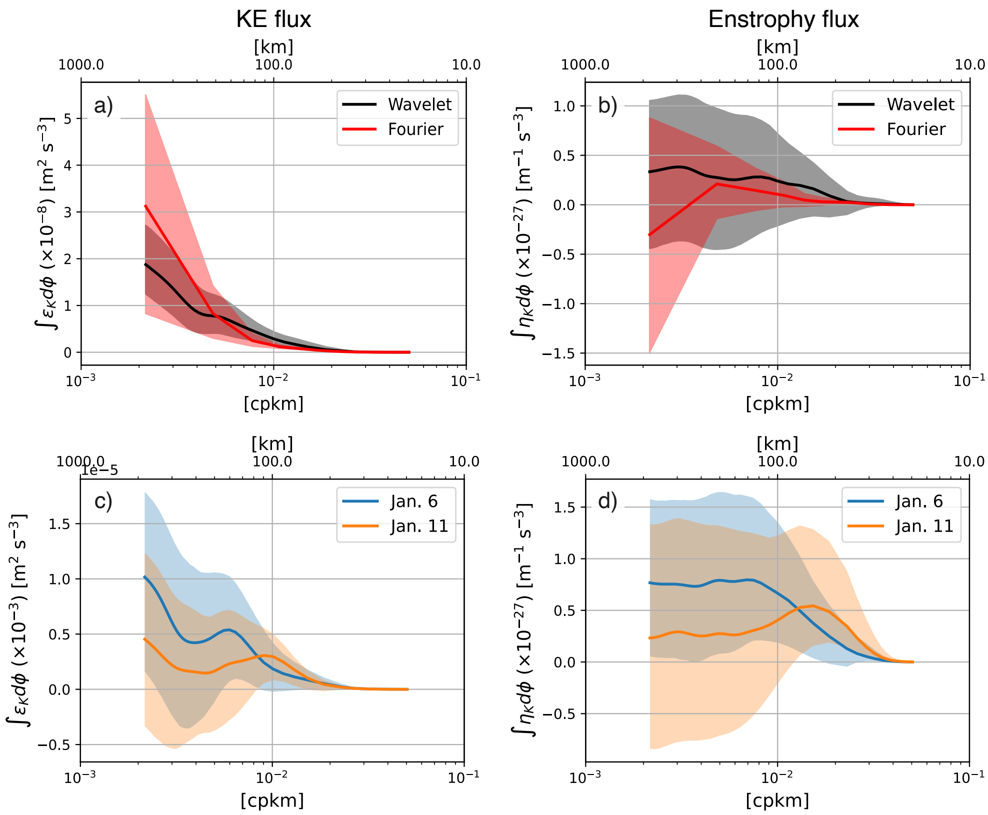

Figure 5. Isotropic (azimuthally-integrated) spectral KE flux ε_K (a), equivalent to A_K integrated in wavenumber, and spectral flux of Ertel's enstrophy η_K at location A from $z = -452\,\mathrm{m}$ on January 1, 1967 (b). The Fourier approach has the land cells interpolated over and is windowed while neither are applied for the wavelet approach. The colored shadings indicate the 95% bootstrap confidence interval. The lower panels show the wavelet spectral flux on Jan. 6 and 11 (c,d).

3.1.4 Implications for spectral scaling

In this section, we review the inertial-range theory within the wavelet approach. We assume for convenience that the mother wavelet is a dimensionless function, in which case the wavelet transform $\tilde{u}$ carries the dimensions L^3T^{-1} and C_Ξ the dimensions L^4. Thus, the dimensions of $\widetilde{E}_K$ are L^3T^{-2}. A cross-scale energy flux ε must have dimensions of L^2T^{-3} and the usual inertial-range arguments lead to

$$\widetilde{E}_K \propto \varepsilon^{2/3} k^{-5/3}\,, \tag{14}$$

in the energy cascade range (Vallis, 2006). In quasi geostrophy, a materially conserved quantity is QG potential vorticity (PV) and its enstrophy flux (η_{QG}) has the dimensions of T^{-3}. If we assume a so-called inertial enstrophy range, characterized by constant enstrophy flux, similar dimensional arguments yield the classical

$$\widetilde{E}_K \propto \eta_{\mathrm{QG}}^{2/3} k^{-3}\,. \tag{15}$$

spectral shape. Accepting the usual QG idea that the enstrophy spectrum is given by $\widetilde{Z}_K = k^2 \widetilde{E}_K(k)$, one obtains a -1 law for the enstrophy spectra.

Here, we consider an extension of these ideas for primitive equations given the observations of spectral slopes steeper than canonical QG estimates (Figs. 3 and 4). Consider an inertial range where the time scale is set, not by ε_K but by η_K, as is assumed for the QG enstrophy cascade range. The presence of an extended range of scales with relatively constant η_K (Fig. 5b,d) is consistent with this assumption. In the richer dynamics of primitive equations, we can write a conservation equation

$$\frac{Dq}{Dt} \approx 0\,, \tag{16}$$

for Ertel's PV $q = \boldsymbol{\omega}\cdot\nabla b = (f+\zeta)b_z + (\boldsymbol{e}_3\times\boldsymbol{u}_z)\cdot\nabla_{\mathrm{h}} b$ where $\boldsymbol{\omega}$ is the absolute vorticity, b buoyancy (detailed in Appendix A), and $\boldsymbol{e}_3$ the vertical unit vector. The horizontal gradients of vertical velocity are neglected consistent with the hydrostatic approximation of our simulation (Vallis, 2006). From a dimensional perspective and material conservation of PV, we argue the units of b are immaterial; it is possible to write a PV equation as (16) where 'b' is replaced by any variable, Θ, such that

$$\frac{D\Theta}{Dt} \approx 0\,, \tag{17}$$

so that surfaces of Θ are nearly material. In the following analysis, we take b to be dimensionless, which is equivalent to buoyancy divided by gravity (hereon noted as $\hat{b} \overset{\mathrm{def}}{=} b/g$ and $q \overset{\mathrm{def}}{=} \boldsymbol{\omega}\cdot\nabla\hat{b}$). Thus, the relevant dimensions of q become $L^{-1}T^{-1}$ and the enstrophy flux (η_{PE}) has dimensions $L^{-2}T^{-3}$. In an inertial range where the time scale is set by a constant PV flux, standard dimensional arguments imply that the energy spectrum should scale as

$$\widetilde{E}_K \propto \eta_{\mathrm{PE}}^{2/3} k^{-13/3}\,, \tag{18}$$

a spectral slope close to -4.3. Due to the richer definition of Ertel's PV compared to QGPV, a simple spectral relation between the KE and enstrophy spectrum does not exist.

We acknowledge that such a steep spectral slope is also achievable by surface quasi geostrophy (SQG) in the interior with varying stratification (Callies & Ferrari, 2013; Yassin & Griffies, 2022). Dimensional analysis only provides a corollary explanation for spectral slopes.

3.2 Spatial dependence of Wavelet spectra in the North Atlantic domain

The wavelet technique agrees well with the Fourier method with the additional strengths of: i) negating the necessity for the data to be periodic, ii) flexibility in defining the wavenumber resolution via the scaling s, and iii) being able to extract the anisotropy in the flow through the rotational matrix R. Given this, we apply our method to five other locations in the North Atlantic subtropical gyre. We take advantage of our wavelet approach in this section; we do not interpolate over land and take the spatial integration (4) by treating them as missing data. As before, there is no need to window the input data on subdomains.

3.2.1 Oriented Spectra

At any spatial location, γ, we compute $\tilde{E}_K(k, \phi)$ for 10 orientation angles. We define energy maximal/minimal angles as those angles resulting in the maximum/minimum integrated energy across all scales in the wavelet decomposition. Plots of the wavelet spectra at energy maximal/minimal wavelet orientation angles, along with the respective angles, are shown for locations A-F in Fig. 6. At all locations, the directions of maximum and minimum energy are nearly orthogonal. The directions closely coincide with the meridional and zonal directions except at locations B and C.

We first examine a location close to the Gulf stream separation point, as seen in Fig. 1 (location A; Fig. 6a), which exhibits the highest energy levels (close to 10^3 $(\mathrm{m}^2\,\mathrm{s}^{-2})$/cpm) amongst all analysed regions. Figures 3a and 6a differ in the land treatment, but also in the fact that the former is azimuthally integrated while the latter is not. A dotted line indicating a -3 slope appears in grey; the spectrum aligned with the angle associated with maximum energy is shallower than the angle associated with minimum energy but still tends to be steeper than -3 at lower wavenumbers, and then transitions to an even steeper decay for higher wavenumbers as already observed in Fig. 3a. A statistically significant signal of anisotropy is apparent, characterized by enhanced energy in the meridional direction relative to the zonal direction. This is likely an imprint of the Gulf Stream on the eddy field due to the roughly zonal orientation of the separated Gulf Stream.

Moving downstream in the North Atlantic Current region (location B; Fig. 6b), the spectral slopes are similar to location A across a wide range except for the smallest wavenumbers. In stark contrast to A, no statistically significant evidence of anisotropy is seen. The spectral amplitudes have dropped from location A by about a factor of three. Location C is roughly from a location on the edge of the so-called 'inertial recirculation' (Fig. 6c). A broad wavenumber band exhibits a steep slope, with best fit line of -4.2, and similarly to location B exhibits little to no evidence of anisotropy. Spectral amplitudes are comparable to those at location B.

The remaining three regions (locations D-F; Fig. 6d-f) come from locations that are ostensibly in the interior of the general circulation, at locations where one might anticipate QG dynamics would govern. Mean flows are weak and do not exhibit much structure on the deformation scale, generating conditions in which isotropy might be anticipated. In accord with these expectations, all three regions have the weakest energy levels, and all are comparable in amplitude. Beyond this, however, the results are quite surprising. Most unexpectedly, all three locations exhibit statistically significant anisotropy, in a sense similar to that at location A. Namely, North-South (nominally) spectra are more energetic than East-West spectra. The spectral slopes are also all steep, and similar to those seen in locations A-C. This is difficult to ascribe to QG dynamics. In short, our quantitative measures of the eddy field in the ocean interior do not meet with our expectations.

Along with the spectra, we exhibit the eddy anisotropy angles defined as (Waterman & Lilly, 2015)

$$\vartheta = \frac{1}{2}\arctan\left(\frac{2\langle u'v'\rangle}{\langle u'^2 - v'^2\rangle}\right) . \tag{19}$$

The angles north of 30°N show no coherent patterns while there is some indication of a slight north-eastward self-organization of angular patterns south of 30°N (Fig. 7), which may be associated to the anisotropy observed in the spectra. We do not exhibit the angle dependency of the spectral flux due to large confidence intervals.

3.2.2 Spectral slopes and fluxes

Beyond the six locations A-F, we exhibit a spatial map of the KE spectral slopes as a least-squares fit between the length scales 250–50 km, and the spectral flux of KE and enstrophy. The wavelet transforms are computed every 5° over a 10°×10° domain.

The spectral slopes below the mixed layer are generally steeper than −3 except for the equatorial region (Fig. 8b). The KE cascade is downscale at the scales of 50 km but starts transitioning to upscale at scales about 200 km and above (Fig. 8c-e). In contrast, the PV-enstrophy consistently cascades downscale across length scales (Fig. 8f-h).

Excluding the non-local term from the KE scale transfer leads to the spectral cascade transitioning to upscale at smaller scales (Fig. 9), which is consistent with previous studies which only examine $\tilde{\boldsymbol{u}'}^* \cdot (\widetilde{\boldsymbol{v} \cdot \nabla \boldsymbol{u}'})$ as the KE scale transfer (e.g. Aluie et al., 2018). Comparing Figs. 8d and 9b, it is interesting that the non-local term only appears significant in the gyre interior but not in the separated Gulf Stream region.

4 Conclusions and discussion

Using a relatively novel wavelet approach applied to an ensemble of eddy-rich North Atlantic simulations, we claim we can compare local spectra from several spots within the general circulation characterized by vastly different dynamics. Specifically, we compare spectra within the recently separated Gulf Stream to those found further downstream, in the inertial recirculation and the gyre interior. The motivation for these comparisons arise from a parameter-free definition of an 'eddy' and interest in clarifying the description of eddies in this heterogeneous field dominated by an ensemble-mean Gulf Stream and relatively quiescent interior. We anticipated that the Gulf Stream would imprint the eddy field with an anisotropic structure, but that the gyre interior would be much simpler and isotropic (Pedlosky et al., 1987). Although an earlier study had warned that the separated Gulf Stream might not be quasi-geostrophic (QG; Jamet et al., 2020), we nonetheless expected to see evidences of up-scale energy cascades at scales beyond the deformation radius, and down-scale cascades at shorter length scales, and that spectral slopes would follow QG expectations.

Several relatively robust characteristics emerge from our calculations, almost none of which aligned with our hypotheses. As expected, the near separation Gulf Stream was found to be anisotropic at the 95% confidence level. However, beyond this, our analysis yielded surprising results. An examination of spectral flux in the near Gulf Stream argued to down scale energy cascades across the spectrum and yielded essentially no evidence for an up-scale flux, although the inverse cascade emerges downstream of the separated Gulf Stream (Fig. 8c,d). Consistent with this, with the caveat of large 95% confidence intervals, was a forward flux of enstrophy (Fig. 8f-h), although our spectral shape was far steeper than the quasi-geostrophically motivated value of -3. This exceptionally steep (~ -4.2) slope was found across all our spectra, including those in the gyre interior where parameterically QG reasoning is expected (Fig. 8b). This steep slope was not sensitive to the numerical viscosity (we examined this by reducing the numerical viscosity by up to two orders of magnitude; not shown). Another unexpected result was the persistence of anisotropy throughout the interior, with exceptions appearing in the far Gulf Stream and the inertial recirculation (Fig. 6).

While we remain largely unable to offer explanations for our results, we have offered some speculations in generalizing the enstrophy inertial-range theory. We can write a potential vorticity (PV) conservation equation for primitive equations, as can be done for a QG system. An unavoidable difference is in the scaling of PV between the two. We argue the dynamically significant difference involves a length scale, which results naturally in a steeper slope. To the extent we can assign dynamics to this, the importance of leading order vortex-tube stretching is emphasized, and this is a phenomenon easily present in the highly stratified Gulf Stream region. The fact that the Ertel's enstrophy flux is positive and relatively constant over a range of wavenumbers where the KE flux varies widely and even changes sign is self consistent with our hypothesis that the eddy turnover time scale may be set by the enstrophy flux (Fig. 8). We remind the reader that the inertial-range theory hinges upon there being a 'constant' flux of something to define the time scale (Kolmogorov, 1941). Its relevance there also underscores, and supports, our earlier analysis suggesting QG dynamics do not adequately describe the separated Gulf Stream (Jamet et al., 2020). What we are unable to explain is the appearance of such steep slopes in locations where QG dynamics are expected to dominate.

In summary, we argue the North Atlantic eddy field is found in an unavoidably inhomogeneous environment (Uchida, Jamet, et al., 2021), and exhibits characteristics that we currently have little theoretical guidance to interpret. The steep spectral slopes could possibly be ascribed to the forward cascade of Ertel's PV, surface quasi geostrophy (SQG) with a varying stratification (Callies & Ferrari, 2013; Yassin & Griffies, 2022), or intermittency in the turbulence cascade (Vallis, 2006). A regime governed by SQG would result in a shoaling of the spectral slope towards the surface, which is what we indeed see from Fig. 8a,b. It is unclear, however, how deep into the real ocean SQG would penetrate as the governing mechanism for turbulence. Further examination on the level of deviation from (surface) quasi geostrophy below the mixed layer is left for future work. The steepness is also likely partially attributable to the lack of submesoscale turbulence in our ensemble, which has been demonstrated to shoal the KE spectra (Capet et al., 2008; Chassignet & Xu, 2017; Ajayi et al., 2020; Khatri et al., 2021), and us analyzing below the surface mixed layer where mixed-layer instability occurs (Boccaletti et al., 2007; Uchida et al., 2019). Amongst the most confusing of our results is the inconsistent appearance and disappearance of anisotropy in our spectra.

The goals of this paper were to apply the wavelet-based technique for estimating the KE spectra and its spectral flux in realistic simulations where the usual assumptions of homogeneity and isotropy are clearly suspect. We have demonstrated that the wavelet method agrees well with the canonical Fourier approach but with the additional strengths of: i) negating the necessity for the data to be periodic, ii) flexibility in defining the wavenumber resolution via the scaling s, and iii) being able to extract the anisotropy in the flow through the rotational matrix R (cf. Uchida, Jamet, et al., 2023). It is also true that the eddy field is not expected to be stationary, although this is a topic that has not received any serious attention in this paper. Based on characteristic time scale arguments $\tau = \widetilde{E}_K/T_K$, one might expect the spectra at scales above 100 km to vary on the timescales of $\sim 10^6$ seconds $\simeq 10$ days looking at Fig. 3a,c. Interestingly, the KE spectra seem remarkably stable over time whereas its tendency T_K fluctuates rapidly with time (Fig. 4). While the ensemble technique permits the examination of the time dependence of eddy spectra, we have only touched upon it here. A more complete examination of the cross-scale eddy energy transfers is also desirable and possible within the ensemble framework. And with it, one can examine in more detail the eddy dynamics to address the question of anisotropic up- and down-scale energy transfers. These are amongst the next set of items we intend to address.

A highly related and separate issue involves the examination of potential energy fluxes. We have here looked solely at the KE spectra. QG theory in its predictions for up and down scale cascades involves the combined kinetic and potential energies of the flow (Vallis, 2006). However, in contrast to QG theory, where the resulting total energy is quadratic and positive definite, primitive equation settings in geopotential coordinates bring no such guarantees as the eddy dynamic enthalpy is a linear term ($h' \stackrel{\text{def}}{=} h - \langle h \rangle$ following the notation by Young, 2010); the TWA framework, on the other hand, suggests a (quadratic) positive-definite total eddy energy when the equation of state for density is linear or when the amplitude of perturbations are on the order of small Rossby number (cf. Loose et al., 2022; Uchida, Jamet, et al., 2022, their Appendix A). How to address the role of potential energy in non-linear cascades and its impact on KE anisotropy is left for future work.

Open Research

The open-source Fourier and wavelet Python packages are available via Github (Uchida, Rokem, et al., 2021; Uchida & Dewar, 2022). Jupyter notebooks used to conduct the analysis are available via Github (`https://github.com/roxyboy/NA-wavelet-notes/tree/master/Snapshots`; a DOI will be added upon acceptance of the manuscript). The simulation outputs are available on the Florida State University cluster (`http://ocean.fsu.edu/~qjamet/share/data/Uchida2021/`).

Acknowledgments

We thank the editor Stephen Griffies along with two anonymous reviewers for their comments, which helped in improving the manuscript. This study is a contribution to the 'Assessing the Role of forced and internal Variability for the Ocean and climate Response in a changing climate' (ARVOR) project supported by the French 'Les Enveloppes Fluides et l'Environnement' (LEFE) program. W. K. Dewar is supported through NSF grants OCE-1829856, OCE-1941963 and OCE-2023585, and the French 'Make Our Planet Great Again' (MOPGA) program managed by the Agence Nationale de la Recherche under the Programme d'Investissement d'Avenir, reference ANR-18-MPGA-0002. The latter two grants served as the primary support for T. Uchida and partially for Q. Jamet. A. Poje acknowledges support from the NSF grant OCE-2123633. High-performance computing resources on Cheyenne (`doi:10.5065/D6RX99HX`) used for running the NA ensembles were provided by NCAR's Computational and Information Systems Laboratory, sponsored by NSF, under the university large allocation UFSU0011. We would like to thank Edward Peirce and Kelly Hirai for maintaining the Florida State University cluster on which the data were analyzed.

Appendix A A dynamically consistent buoyancy

For primitive equation models employing a non-linear equation of state (Jackett & McDougall, 1995), the choice of a materially conserved buoyancy variable is non-trivial and has been a subject of debate (e.g. Montgomery, 1937; Jackett & McDougall, 1997; McDougall & Jackett, 2005; de Szoeke & Springer, 2009; Klocker et al., 2009; Tailleux, 2016a, 2016b, 2017, 2021; McDougall et al., 2017; Lang et al., 2020; Stanley et al., 2021). Following Stanley (2019), Stanley and Marshall (2022) and Uchida, Jamet, et al. (2022), we opt for in-situ density anomaly to define the buoyancy $\hat{b} = -\delta/\rho_0$ where $\rho_0 = 999.8\,\mathrm{kg\,m^{-3}}$ is the Boussinesq reference density prescribed in MITgcm and kept dimensionless (cf. Section 3.1.4). The in-situ density anomaly $\delta\,(= \rho - \breve{\rho})$ is defined by removing the effect of compressibility while retaining a straightforward dynamical relation to the horizontal gradients of hydrostatic pressure in Boussinesq fluids; this relation is crucial for dynamical consistency in how buoyancy relates to momentum. Taking $\mathcal{C}_s(z)$ as the maximum sound speed at each depth over the entire model domain and ensemble, we define $\breve{\rho}$ as:

$$\breve{\rho}(z) = -\int_z^0 \frac{\rho_0 g}{\mathcal{C}_s} dz + \rho_0, \tag{A1}$$

which reduces to $\breve{\rho}\big|_{z=0} = \rho_0$. δ is subsequently diagnosed as the difference between the in-situ density and $\breve{\rho}$. The interested reader is referred to Uchida, Jamet, et al. (2022) for further details. While more elaborate techniques may improve the material conservation of δ (and hence b), the relation to the dynamics is non-trivial for other density variables such as omega, neutral, orthobaric and topological density surfaces (Jackett & McDougall, 1997; McDougall & Jackett, 2005; Klocker et al., 2009; Stanley, 2019).

Appendix B Spectral budget of the eddy flow

One of the desirable properties of taking the averaging over the ensemble dimension is that the wavelet transform and averaging operator commute with each other, i.e. $\langle \widetilde{\cdot} \rangle = \widetilde{\langle \cdot \rangle}$, owing to the ensemble dimension being orthogonal to the spatiotemporal dimensions.

B1 Eddy kinetic energy

The ensemble mean kinetic energy (KE; $K^{\#} = |\langle \boldsymbol{u} \rangle|^2/2$) equation is given as

$$K_t^{\#} + \langle \boldsymbol{v} \rangle \cdot \nabla K^{\#} = -\langle \boldsymbol{u} \rangle \cdot \nabla_{\mathrm{h}} \langle \phi \rangle - \langle u \rangle \nabla \cdot \langle \boldsymbol{v}' u' \rangle - \langle v \rangle \nabla \cdot \langle \boldsymbol{v}' v' \rangle + \langle \boldsymbol{u} \rangle \cdot \langle \boldsymbol{\mathcal{K}} \rangle \tag{B1}$$

where $\boldsymbol{v} = \boldsymbol{u} + w\boldsymbol{e}_3$ is the three-dimensional velocity, and $\boldsymbol{\mathcal{K}}$ is the non-conservative term consisting of dissipation and contribution from KPP. The total KE, on the other hand, is

$$K_t + \boldsymbol{v} \cdot \nabla K = -\boldsymbol{u} \cdot \nabla_{\mathrm{h}} \phi + \boldsymbol{u} \cdot \boldsymbol{\mathcal{K}} . \tag{B2}$$

Now, the total KE can be expanded as

$$\begin{aligned} K &= \frac{1}{2} |\langle \boldsymbol{u} \rangle + \boldsymbol{u}'|^2 \\ &= K^{\#} + \mathscr{K} + \langle \boldsymbol{u} \rangle \cdot \boldsymbol{u}' , \end{aligned} \tag{B3}$$

where $\mathscr{K} = |\boldsymbol{u}'|^2/2$ so

$$\begin{aligned} \langle \boldsymbol{v} \cdot \nabla K \rangle &= \big\langle (\langle \boldsymbol{v} \rangle + \boldsymbol{v}') \cdot \nabla (K^{\#} + \mathscr{K} + \langle \boldsymbol{u} \rangle \cdot \boldsymbol{u}') \big\rangle \\ &= \langle \boldsymbol{v} \rangle \cdot \nabla K^{\#} + \langle \boldsymbol{v}' \cdot \nabla \mathscr{K} \rangle + \langle \boldsymbol{v} \rangle \cdot \nabla \langle \mathscr{K} \rangle + \langle \boldsymbol{v}' \cdot \nabla (\langle \boldsymbol{u} \rangle \cdot \boldsymbol{u}') \rangle \; . \end{aligned} \tag{B4}$$

Hence, subtracting (B1) from the ensemble mean of (B2) yields

$$\langle \mathscr{K} \rangle_t = -\langle \boldsymbol{u}' \cdot \nabla_{\mathrm{h}} \phi' \rangle - \langle \boldsymbol{v} \cdot \nabla \mathscr{K} \rangle - \langle \boldsymbol{v}' \cdot \nabla (\langle \boldsymbol{u} \rangle \cdot \boldsymbol{u}') \rangle + \langle u \rangle \nabla \cdot \langle \boldsymbol{v}' u' \rangle + \langle v \rangle \nabla \cdot \langle \boldsymbol{v}' v' \rangle + \langle \boldsymbol{u}' \cdot \boldsymbol{\mathcal{K}}' \rangle , \tag{B5}$$

where we see the mean flow and eddies exchanging energy via the term $\langle u \rangle \nabla \cdot \langle \boldsymbol{v}' u' \rangle + \langle v \rangle \nabla \cdot \langle \boldsymbol{v}' v' \rangle$, which can be interpreted as a eddy forcing onto the mean flow.

In order to achieve machine precision in closing the budget using the MITgcm `diagnostics` package outputs, we rearrange Equation (B5) as

$$\begin{aligned} \langle \mathscr{K} \rangle_t = &-\langle \boldsymbol{u}' \cdot \nabla_{\mathrm{h}} \phi' \rangle - \langle \boldsymbol{v} \cdot \nabla \mathscr{K} \rangle - \underbrace{\left(\langle u' \boldsymbol{v}' \rangle \cdot \nabla \langle u \rangle + \langle v' \boldsymbol{v}' \rangle \cdot \nabla \langle v \rangle + \langle u \rangle \nabla \cdot \langle \boldsymbol{v}' u' \rangle + \langle v \rangle \nabla \cdot \langle \boldsymbol{v}' v' \rangle \right)}_{= \langle \boldsymbol{v}' \cdot \nabla (\langle \boldsymbol{u} \rangle \cdot \boldsymbol{u}') \rangle} \\ &+ \langle u \rangle \nabla \cdot \langle \boldsymbol{v}' u' \rangle + \langle v \rangle \nabla \cdot \langle \boldsymbol{v}' v' \rangle + \langle \boldsymbol{u}' \cdot \boldsymbol{\mathcal{K}}' \rangle \\ = &-\langle \boldsymbol{u}' \cdot \nabla_{\mathrm{h}} \phi' \rangle - \underbrace{\left(\langle u' (\boldsymbol{v} \cdot \nabla u)' \rangle + \langle v' (\boldsymbol{v} \cdot \nabla v)' \rangle + \langle u \rangle \nabla \cdot \langle \boldsymbol{v}' u' \rangle + \langle v \rangle \nabla \cdot \langle \boldsymbol{v}' v' \rangle \right)}_{= \langle \boldsymbol{v} \cdot \nabla \mathscr{K} \rangle + \langle \boldsymbol{v}' \cdot \nabla (\langle \boldsymbol{u} \rangle \cdot \boldsymbol{u}') \rangle} \\ &+ \langle u \rangle \nabla \cdot \langle \boldsymbol{v}' u' \rangle + \langle v \rangle \nabla \cdot \langle \boldsymbol{v}' v' \rangle + \langle \boldsymbol{u}' \cdot \boldsymbol{\mathcal{K}}' \rangle , \end{aligned}$$

where we have also grouped all the divergence terms together as they are neither a source nor sink of energy and only redistribute it. The spectral budget of eddy KE, therefore, becomes

$$\underbrace{\frac{1}{C_\Xi}\langle\tilde{\boldsymbol{u}'}^* \cdot \tilde{\boldsymbol{u}'_t}\rangle\, x_0^2 k}_{T_K} = \underbrace{-\frac{1}{C_\Xi}\langle\tilde{\boldsymbol{u}'}^* \cdot \widetilde{\nabla_\mathrm{h}\phi'}\rangle\, x_0^2 k}_{P_K}$$
$$\underbrace{-\frac{1}{C_\Xi}\left(\langle\tilde{u'}^*(\widetilde{\boldsymbol{v}\cdot\nabla u})'\rangle + \langle\tilde{v'}^*(\widetilde{\boldsymbol{v}\cdot\nabla v})'\rangle + \widetilde{\langle u\rangle}^*\widetilde{\nabla\cdot\langle\boldsymbol{v}'u'\rangle} + \widetilde{\langle v\rangle}^*\widetilde{\nabla\cdot\langle\boldsymbol{v}'v'\rangle}\right) x_0^2 k}_{A_K}$$
$$+ \underbrace{\frac{1}{C_\Xi}\left(\widetilde{\langle u\rangle}^*\widetilde{\nabla\cdot\langle\boldsymbol{v}'u'\rangle} + \widetilde{\langle v\rangle}^*\widetilde{\nabla\cdot\langle\boldsymbol{v}'v'\rangle}\right) x_0^2 k}_{\mathrm{MtE}_K} + \underbrace{\frac{1}{C_\Xi}\langle\tilde{\boldsymbol{u}'}^* \cdot \widetilde{\boldsymbol{\mathcal{K}}'}\rangle\, x_0^2 k}_{\mathcal{K}_K}\,, \quad \text{(B6)}$$

(cf. (10)) where MtE_K is the KE exchange between the mean and eddy flow. C_Ξ is computed using the `xrft` Python package (Uchida, Rokem, et al., 2021). The horizontal KE spectral flux often examined by other studies is encapsulated in A_K of (B6).

B2 Eddy enstrophy

The enstrophy equation is slightly more tractable than the KE equation so we start off with the mean and eddy Ertel's PV equations neglecting the non-conservative terms

$$\langle q\rangle_t + \nabla\cdot(\langle\boldsymbol{v}\rangle\langle q\rangle) = -\nabla\cdot\langle\boldsymbol{v}'q'\rangle\,, \quad \text{(B7)}$$

$$q'_t + \nabla\cdot(\boldsymbol{v}q') + \nabla\cdot(\boldsymbol{v}'\langle q\rangle) = \nabla\cdot\langle\boldsymbol{v}'q'\rangle\,, \quad \text{(B8)}$$

where the mean flow and eddies exchange PV via the term $\nabla\cdot\langle\boldsymbol{v}'q'\rangle$. Multiplying each by $\langle q\rangle$ and q' and taking the ensemble mean gives the mean and eddy enstrophy equations

$$\langle q\rangle\langle q\rangle_t + \langle q\rangle\nabla\cdot(\langle\boldsymbol{v}\rangle\langle q\rangle) = -\langle q\rangle\nabla\cdot\langle\boldsymbol{v}'q'\rangle\,, \quad \text{(B9)}$$

$$\langle q'q'_t\rangle + \langle q'\nabla\cdot(\boldsymbol{v}q')\rangle + \underbrace{\langle q'\nabla\cdot(\boldsymbol{v}'\langle q\rangle)\rangle}_{=\langle\boldsymbol{v}'\cdot\nabla(\langle q\rangle q')\rangle - \langle q\rangle\nabla\cdot\langle\boldsymbol{v}'q'\rangle} = 0\,. \quad \text{(B10)}$$

In a similar manner to the EKE equation, the eddy enstrophy equation can also be rearranged as

$$\langle q'q'_t\rangle + \underbrace{\langle q'(\boldsymbol{v}\cdot\nabla q)'\rangle + \langle q\rangle\nabla\cdot\langle\boldsymbol{v}'q'\rangle}_{=\langle q'\nabla\cdot(\boldsymbol{v}q')\rangle + \langle\boldsymbol{v}'\cdot\nabla(\langle q\rangle q')\rangle} = \langle q\rangle\nabla\cdot\langle\boldsymbol{v}'q'\rangle\,. \quad \text{(B11)}$$

Thus, the eddy enstrophy budget in wavelet domain becomes

$$\frac{1}{C_\Xi}\langle\tilde{q'}^*\tilde{q'_t}\rangle x_0^2 k + \frac{1}{C_\Xi}\left[\langle\tilde{q'}^*(\widetilde{\nabla\cdot\boldsymbol{v}q})'\rangle + \widetilde{\langle q\rangle}^*\widetilde{\nabla\cdot\langle\boldsymbol{v}'q'\rangle}\right] x_0^2 k = \frac{1}{C_\Xi}\widetilde{\langle q\rangle}^*\widetilde{\nabla\cdot\langle\boldsymbol{v}'q'\rangle} x_0^2 k\,. \quad \text{(B12)}$$

We note that the enstrophy budget does not close to machine precision due to the lack of `diagnostics` outputs.

References

Ajayi, A., Le Sommer, J., Chassignet, E., Molines, J., Xu, X., Albert, A., & Dewar, W. (2021). Diagnosing cross-scale kinetic energy exchanges from two submesoscale permitting ocean models. *Journal of Advances in Modeling Earth Systems*. doi: 10.1029/2019MS001923

Ajayi, A., Le Sommer, J., Chassignet, E., Molines, J.-M., Xu, X., Albert, A., & Cosme, E. (2020). Spatial and temporal variability of the north atlantic eddy field from two kilometric-resolution ocean models. *Journal of Geophysical Research: Oceans*, *125*(5), e2019JC015827. doi: 10.1029/2019JC015827

Aluie, H., Hecht, M., & Vallis, G. (2018). Mapping the energy cascade in the North Atlantic Ocean: The coarse-graining approach. *Journal of Physical Oceanography*, *48*, 225-244. doi: 10.1175/JPO-D-17-0100.1

Aoki, K. (2014). A constraint on the thickness-weighted average equation of motion deduced from energetics. *Journal of Marine Research*, *72*, 355-382. doi: 10.1357/002224014815469886

Arbic, B. K., Polzin, K. L., Scott, R. B., Richman, J. G., & Shriver, J. F. (2013). On eddy viscosity, energy cascades, and the horizontal resolution of gridded satellite altimeter products. *Journal of Physical Oceanography*, *43*(2), 283–300. doi: 10.1175/JPO-D-11-0240.1

Beech, N., Rackow, T., Semmler, T., Danilov, S., Wang, Q., & Jung, T. (2022). Long-term evolution of ocean eddy activity in a warming world. *Nature climate change*, *12*(10), 910–917. doi: 10.1038/s41558-022-01478-3

Berloff, P., Ryzhov, E., & Shevchenko, I. (2021). On dynamically unresolved oceanic mesoscale motions. *Journal of Fluid Mechanics*. doi: 10.1017/jfm.2021.477

Boccaletti, G., Ferrari, R., & Fox-Kemper, B. (2007). Mixed layer instabilities and restratification. *Journal of Physical Oceanography*, *37*(9), 2228–2250.

Callies, J., & Ferrari, R. (2013). Interpreting energy and tracer spectra of upper-ocean turbulence in the submesoscale range (1–200 km). *Journal of Physical Oceanography*, *43*(11), 2456–2474. doi: 10.1175/JPO-D-13-063.1

Campagne, A., Gallet, B., Moisy, F., & Cortet, P.-P. (2014). Direct and inverse energy cascades in a forced rotating turbulence experiment. *Physics of Fluids*, *26*(12), 125112. doi: 10.1063/1.4904957

Capet, X., McWilliams, J. C., Molemaker, M. J., & Shchepetkin, A. F. (2008).

Mesoscale to submesoscale transition in the california current system. Part I: Flow structure, eddy flux, and observational tests. *Journal of Physical Oceanography*, *38*(1), 29–43. doi: 10.1175/2007JPO3671.1

Charney, J. G. (1971). Geostrophic turbulence. *Journal of the Atmospheric Sciences*, *28*(6), 1087–1095. doi: 10.1175/1520-0469(1971)028⟨1087:GT⟩2.0.CO;2

Chassignet, E. P., & Marshall, D. P. (2008). Gulf Stream separation in numerical ocean models. *Geophysical Monograph Series*, *177*. doi: 10.1029/177GM05

Chassignet, E. P., & Xu, X. (2017). Impact of horizontal resolution (1/12°to 1/50°) on Gulf Stream separation, penetration, and variability. *Journal of Physical Oceanography*, *47*, 1999-2021. doi: 10.1175/JPO-D-17-0031.1

Chassignet, E. P., Yeager, S. G., Fox-Kemper, B., Bozec, A., Castruccio, F., Danabasoglu, G., ... others (2020). Impact of horizontal resolution on global ocean–sea ice model simulations based on the experimental protocols of the Ocean Model Intercomparison Project phase 2 (OMIP-2). *Geoscientific Model Development*, *13*(9), 4595–4637. doi: 10.5194/gmd-13-4595-2020

Chen, R., & Flierl, G. R. (2015). The contribution of striations to the eddy energy budget and mixing: Diagnostic frameworks and results in a quasigeostrophic barotropic system with mean flow. *Journal of Physical Oceanography*, *45*(8), 2095–2113. doi: 10.1175/JPO-D-14-0199.1

Constantinou, N. C., & Hogg, A. M. (2021). Intrinsic oceanic decadal variability of upper-ocean heat content. *Journal of Climate*, 1–42. doi: 10.1175/JCLI-D-20-0962.1

Daubechies, I. (1992). *Ten lectures on wavelets*. SIAM.

de Szoeke, R. A., & Springer, S. R. (2009). The materiality and neutrality of neutral density and orthobaric density. *Journal of Physical Oceanography*, *39*(8), 1779–1799. doi: 10.1175/2009JPO4042.1

Dewar, W. K., Parfitt, R., & Wienders, N. (2022). Routine reversal of the AMOC in an ocean model ensemble. *Geophysical Research Letters*, e2022GL100117. doi: 10.1029/2022GL100117

Gabor, D. (1946). Theory of communication. Part 1: The analysis of information. *Journal of the Institution of Electrical Engineers-Part III: Radio and Communication Engineering*, *93*(26), 429–441.

Gage, K. S., & Nastrom, G. D. (1986). Theoretical interpretation of atmospheric wavenumber spectra of wind and temperature observed by commercial aircraft during GASP. *Journal of Atmospheric Sciences*, *43*(7), 729–740. doi: 10.1175/1520-0469(1986)043⟨0729:TIOAWS⟩2.0.CO;2

Gent, P. R. (2011). The Gent–McWilliams parameterization: 20/20 hindsight. *Ocean Modelling*, *39*(1-2), 2–9. doi: 10.1016/j.ocemod.2010.08.002

Gent, P. R., & Mcwilliams, J. C. (1990). Isopycnal mixing in ocean circulation models. *Journal of Physical Oceanography*, *20*(1), 150–155. doi: 10.1175/1520-0485(1990)020⟨0150:IMIOCM⟩2.0.CO;2

Germe, A., Hirschi, J. J.-M., Blaker, A. T., & Sinha, B. (2022). Chaotic variability of the atlantic meridional overturning circulation at subannual time scales. *Journal of Physical Oceanography*, *52*(5), 929–949. doi: 10.1175/JPO-D-21-0100.1

Griffies, S. M., Winton, M., Anderson, W. G., Benson, R., Delworth, T. L., Dufour, C. O., ... others (2015). Impacts on ocean heat from transient mesoscale eddies in a hierarchy of climate models. *Journal of Climate*, *28*(3), 952–977. doi: 10.1175/JCLI-D-14-00353.1

Guillaumin, A. P., & Zanna, L. (2021). Stochastic-deep learning parameterization of ocean momentum forcing. *Journal of Advances in Modeling Earth Systems*, *13*(9), e2021MS002534. doi: 10.1029/2021MS002534

Held, I. M., Pierrehumbert, R. T., Garner, S. T., & Swanson, K. L. (1995). Surface quasi-geostrophic dynamics. *Journal of Fluid Mechanics*, *282*, 1–20. doi: 10.1017/S0022112095000012

Jackett, D. R., & McDougall, T. J. (1995). Minimal adjustment of hydrographic profiles to achieve static stability. *Journal of Atmospheric and Oceanic Technology*, *12*, 381-389.

Jackett, D. R., & McDougall, T. J. (1997). A neutral density variable for the world's oceans. *Journal of Physical Oceanography*, *27*(2), 237–263. doi: 10.1175/1520-0485(1997)027⟨0237:ANDVFT⟩2.0.CO;2

Jamet, Q., Deremble, B., Wienders, N., Uchida, T., & Dewar, W. K. (2020). On wind-driven energetics of subtropical gyres. *Journal of Advances in Modeling Earth Systems*, *13*(4), e2020MS002329. doi: 10.1029/2020MS002329

Jamet, Q., Dewar, W. K., Wienders, N., & Deremble, B. (2019). Spatio-temporal patterns of chaos in the Atlantic Overturning Circulation. *Geophysical Re-*

search Letters, doi: 10.1029/2019GL082552.

Jamet, Q., Leroux, S., Dewar, W. K., Penduff, T., Le Sommer, J., Molines, J.-M., & Gula, J. (2022). Non-local eddy-mean kinetic energy transfers in submesoscale-permitting ensemble simulations. *Journal of Advances in Modeling Earth Systems*. doi: 10.1029/2022MS003057

Jansen, M. F., Adcroft, A., Khani, S., & Kong, H. (2019). Toward an energetically consistent, resolution aware parameterization of ocean mesoscale eddies. *Journal of Advances in Modeling Earth Systems*, *11*(8), 2844–2860. doi: 10.1029/2019MS001750

Kay, J. E., Deser, C., Phillips, A., Mai, A., Hannay, C., Strand, G., … others (2015). The Community Earth System Model (CESM) large ensemble project: A community resource for studying climate change in the presence of internal climate variability. *Bulletin of the American Meteorological Society*, *96*(8), 1333–1349. doi: 10.1175/BAMS-D-13-00255.1

Khatri, H., Griffies, S. M., Uchida, T., Wang, H., & Menemenlis, D. (2021). Role of mixed-layer instabilities in the seasonal evolution of eddy kinetic energy spectra in a global submesoscale permitting simulation. *Geophysical Research Letters*, *48*(18), e2021GL094777. doi: 10.1029/2021GL094777

Khatri, H., Sukhatme, J., Kumar, A., & Verma, M. K. (2018). Surface ocean enstrophy, kinetic energy fluxes, and spectra from satellite altimetry. *Journal of Geophysical Research: Oceans*, *123*(5), 3875–3892. doi: 10.1029/2017JC013516

Klocker, A., McDougall, T. J., & Jackett, D. R. (2009). A new method for forming approximately neutral surfaces. *Ocean Science*, *5*(2), 155–172. doi: 10.5194/os-5-155-2009

Kolmogorov, A. (1941). The local structure of turbulence in incompressible viscous fluid for very large Reynolds numbers. *C R Academy of Sciences URSS*, *30*, 301-305.

Lang, Y., Stanley, G. J., McDougall, T. J., & Barker, P. M. (2020). A pressure-invariant neutral density variable for the World's Oceans. *Journal of Physical Oceanography*, 1–58. doi: 10.1175/JPO-D-19-0321.1

Lapeyre, G. (2017). Surface quasi-geostrophy. *Fluids*, *2*(1), 7. doi: 10.3390/fluids2010007

Large, W., McWilliams, J., & Doney, S. (1994). Oceanic vertical mixing: A review and a model with a nonlocal boundary layer parameterization. *Reviews of Geophysics*, *32*, 363-403.

Leroux, S., Brankart, J.-M., Albert, A., Brodeau, L., Molines, J.-M., Jamet, Q., … Brasseur, P. (2022). Ensemble quantification of short-term predictability of the ocean dynamics at a kilometric-scale resolution: a Western Mediterranean test case. *Ocean Science*, *18*(6), 1619–1644. doi: 10.5194/os-18-1619-2022

Leroux, S., Penduff, T., Bessières, L., Molines, J.-M., Brankart, J.-M., Sérazin, G., … Terray, L. (2018). Intrinsic and atmospherically forced variability of the AMOC: Insights from a large-ensemble ocean hindcast. *Journal of Climate*, *31*(3), 1183–1203. doi: 10.1175/JCLI-D-17-0168.1

Li, L., Deremble, B., Lahaye, N., & Mémin, E. (2023). Stochastic data-driven parameterization of unresolved eddy effects in a baroclinic quasi-geostrophic model. *Journal of Advances in Modeling Earth Systems*, *15*(2), e2022MS003297. doi: 10.1029/2022MS003297

Loose, N., Bachman, S., Grooms, I., & Jansen, M. (2022). Diagnosing scale-dependent energy cycles in a high-resolution isopycnal ocean model. *Journal of Physical Oceanography*, *53*(1), 157–176. doi: 10.1175/JPO-D-22-0083.1

Lorenz, E. N. (1963). Deterministic nonperiodic flow. *Journal of atmospheric sciences*, *20*(2), 130–141. doi: 10.1175/1520-0469(1963)020⟨0130:DNF⟩2.0.CO;2

Maher, N., Milinski, S., Suarez-Gutierrez, L., Botzet, M., Dobrynin, M., Kornblueh, L., … others (2019). The Max Planck Institute Grand Ensemble: Enabling the exploration of climate system variability. *Journal of Advances in Modeling Earth Systems*, *11*(7), 2050–2069. doi: 10.1029/2019MS001639

Marshall, D., Maddison, J., & Berloff, P. (2012). A framework for parameterizing eddy potential vorticity fluxes. *Journal of Physical Oceanography*, *42*, 539-557.

McDougall, T. J., Groeskamp, S., & Griffies, S. M. (2017). Comment on Tailleux, R. Neutrality versus materiality: A thermodynamic theory of neutral surfaces. Fluids 2016, 1, 32. *Fluids*, *2*(2), 19. doi: 10.3390/fluids2020019

McDougall, T. J., & Jackett, D. R. (2005). An assessment of orthobaric density in the global ocean. *Journal of Physical Oceanography*, *35*(11), 2054–2075. doi: 10.1175/JPO2796.1

Meunier, J., Miquel, B., & Gallet, B. (2023). A direct derivation of the gent–

mcwilliams/redi diffusion tensor from quasi-geostrophic dynamics. *Journal of Fluid Mechanics*, *963*, A22. doi: 10.1017/jfm.2023.347

Montgomery, R. (1937). A suggested method for representing gradient flow in isentropic surfaces. *Bulletin of the American Meteorological Society*, *18,*, 210-212. Retrieved from `http://www.jstor.org/stable/26263980`

Morlet, J., Arens, G., Fourgeau, E., & Glard, D. (1982). Wave propagation and sampling theory—Part I: Complex signal and scattering in multilayered media. *Geophysics*, *47*(2), 203–221. doi: 10.1190/1.1441328

Pedlosky, J., et al. (1987). *Geophysical fluid dynamics* (Vol. 710). Springer.

Perrier, V., Philipovitch, T., & Basdevant, C. (1995). Wavelet spectra compared to Fourier spectra. *Journal of mathematical physics*, *36*(3), 1506–1519. doi: 10.1063/1.531340

Poincaré, H. (1890). On the three-body problem and the equations of dynamics. *Acta Math*, *13*(1).

Redi, M. H. (1982). Oceanic isopycnal mixing by coordinate rotation. *Journal of Physical Oceanography*, *12*(10), 1154–1158. doi: 10.1175/1520-0485(1982)012⟨1154:OIMBCR⟩2.0.CO;2

Rocha, C. B., Chereskin, T. K., Gille, S. T., & Menemenlis, D. (2016). Mesoscale to submesoscale wavenumber spectra in Drake Passage. *Journal of Physical Oceanography*, *46*(2), 601–620. doi: 10.1175/JPO-D-15-0087.1

Romanou, A., Rind, D., Jonas, J., Miller, R., Kelley, M., Russell, G., … Schmidt, G. A. (2023). Stochastic bifurcation of the North Atlantic Circulation under a mid-range future climate scenario with the NASA-GISS modelE. *Journal of Climate*, 1–49. doi: 10.1175/JCLI-D-22-0536.1

Saba, V. S., Griffies, S. M., Anderson, W. G., Winton, M., Alexander, M. A., Delworth, T. L., … others (2016). Enhanced warming of the Northwest Atlantic Ocean under climate change. *Journal of Geophysical Research: Oceans*, *121*(1), 118–132. doi: 10.1002/2015JC011346

Scott, R., & Wang, F. (2005). Direct evidence of an oceanic inverse kinetic energy cascade from satellite altimetry. *Journal of Physical Oceanography*, *35*, 1650-1666. doi: 10.1175/JPO2771.1

Sérazin, G., Jaymond, A., Leroux, S., Penduff, T., Bessières, L., Llovel, W., … Terray, L. (2017). A global probabilistic study of the ocean heat content lowfrequency variability: Atmospheric forcing versus oceanic chaos. *Geophysical Research Letters*, *44*(11), 5580–5589. doi: 10.1002/2017GL073026

Stainforth, D. A., Allen, M. R., Tredger, E. R., & Smith, L. A. (2007). Confidence, uncertainty and decision-support relevance in climate predictions. *Philosophical Transactions of the Royal Society A: Mathematical, Physical and Engineering Sciences*, *365*(1857), 2145–2161. doi: 10.1098/rsta.2007.2074

Stammer, D. (1998). On eddy characteristics, eddy transports, and mean flow properties. *Journal of Physical Oceanography*, *28*(4), 727–739. doi: 10.1175/1520-0485(1998)028⟨0727:OECETA⟩2.0.CO;2

Stammer, D., & Wunsch, C. (1999). Temporal changes in eddy energy of the oceans. *Deep Sea Research Part II: Topical Studies in Oceanography*, *46*(1-2), 77–108. doi: 10.1016/S0967-0645(98)00106-4

Stanley, G. J. (2019). Neutral surface topology. *Ocean Modelling*, *138*, 88–106. doi: 10.1016/j.ocemod.2019.01.008

Stanley, G. J., & Marshall, D. P. (2022). Why mean potential vorticity cannot be materially conserved in the eddying Southern Ocean. *Journal of Physical Oceanography*. doi: 10.1175/JPO-D-21-0195.1

Stanley, G. J., McDougall, T. J., & Barker, P. M. (2021). Algorithmic improvements to finding approximately neutral surfaces. *Journal of Advances in Modeling Earth Systems*, *13*(5), e2020MS002436. doi: 10.1029/2020MS002436

Tailleux, R. (2016a). Generalized patched potential density and thermodynamic neutral density: Two new physically based quasi-neutral density variables for ocean water masses analyses and circulation studies. *Journal of Physical Oceanography*, *46*(12), 3571–3584. doi: 10.1175/JPO-D-16-0072.1

Tailleux, R. (2016b). Neutrality versus materiality: A thermodynamic theory of neutral surfaces. *Fluids*, *1*(4), 32. doi: 10.3390/fluids1040032

Tailleux, R. (2017). Reply to "Comment on Tailleux, R. Neutrality Versus Materiality: A Thermodynamic Theory of Neutral Surfaces. Fluids 2016, 1, 32.". *Fluids*, *2*(2), 20. doi: 10.3390/fluids2020020

Tailleux, R. (2021). Spiciness theory revisited, with new views on neutral density, orthogonality, and passiveness. *Ocean Science*, *17*(1), 203–219. doi: 10.5194/os-17-203-2021

Uchida, T., Abernathey, R., & Smith, S. (2017). Seasonality of eddy kinetic energy in an eddy permitting global climate model. *Ocean Modelling*, *118*, 41–58. doi: 10.1016/j.ocemod.2017.08.006

Uchida, T., Balwada, D., Abernathey, R., McKinley, G., Smith, S., & Lévy, M. (2019). The contribution of submesoscale over mesoscale eddy iron transport in the open Southern Ocean. *Journal of Advances in Modeling Earth Systems*, *11*(12), 3934–3958. doi: 10.1029/2019MS001805

Uchida, T., Balwada, D., Jamet, Q., Dewar, W. K., Deremble, B., Penduff, T., & Le Sommer, J. (2023). Cautionary tales from the mesoscale eddy transport tensor. *Ocean Modelling*. doi: 10.1016/j.ocemod.2023.102172

Uchida, T., Deremble, B., Dewar, W. K., & Penduff, T. (2021). Diagnosing the Eliassen-Palm flux from a quasi-geostrophic double gyre ensemble. In *Earthcube annual meeting.* Retrieved from `https://earthcube2021.github.io/ec21_book/notebooks/ec21_uchida_etal/notebooks/TU_05_Diagnosing-the-Eliassen-Palm-flux-from-a-quasi-geostrophic-double-gyre-ensemble.html` doi: 10.5281/zenodo.5496375

Uchida, T., Deremble, B., & Penduff, T. (2021). The seasonal variability of the ocean energy cycle from a quasi-geostrophic double gyre ensemble. *Fluids*, *6*(6), 206. doi: 10.3390/fluids6060206

Uchida, T., Deremble, B., & Popinet, S. (2022). Deterministic model of the eddy dynamics for a midlatitude ocean model. *Journal of Physical Oceanography*. doi: 10.1175/JPO-D-21-0217.1

Uchida, T., & Dewar, W. K. (2022). `xwavelet`*: Wavelet transforms for xarray data [Software].* doi: 10.5281/zenodo.6022738

Uchida, T., Jamet, Q., Dewar, W. K., Balwada, D., Le Sommer, J., & Penduff, T. (2022). Diagnosing the thickness-weighted averaged eddy-mean flow interaction in an eddying North Atlantic ensemble: The Eliassen–Palm flux. *Journal of Advances in Modeling Earth Systems*. doi: 10.1029/2021MS002866

Uchida, T., Jamet, Q., Poje, A., & Dewar, W. K. (2021). An ensemble-based eddy and spectral analysis, with application to the Gulf Stream. *Journal of Advances in Modeling Earth Systems*, e2021MS002692. doi: 10.1029/2021MS002692

Uchida, T., Jamet, Q., Poje, A., Wienders, N., Dewar, W., & Deremble, B. (2023). Wavelet-based wavenumber spectral estimate of eddy kinetic energy: Idealized quasi-geostrophic flow. *Journal of Advances in Modeling Earth Systems*, *15*(3). doi: 10.1029/2022MS003399

Uchida, T., Rokem, A., Squire, D., Nicholas, T., Abernathey, R. P., Soler, S., ... others (2021). `xrft`*: Fourier transforms for xarray data [Software].* Retrieved from `https://xrft.readthedocs.io/en/latest/` doi: 10.5281/zenodo.1402635

Vallis, G. (2006). *Atmospheric and Oceanic Fluid Dynamics.* Cambridge.

Vergara, O., Morrow, R., Pujol, I., Dibarboure, G., & Ubelmann, C. (2019). Revised global wavenumber spectra from recent altimeter observations. *Journal of Geophysical Research: Oceans*, *124*(6), 3523–3537. doi: 10.1029/2018JC014844

Waterman, S., & Lilly, J. M. (2015). Geometric decomposition of eddy feedbacks in barotropic systems. *Journal of Physical Oceanography*, *45*(4), 1009–1024. doi: 10.1175/JPO-D-14-0177.1

Wunsch, C. (1981). The Evolution of Physical Oceanography: Scientific Surveys in Honor of Henry Stommel. In C. Wunsch & B. Warren (Eds.), (p. 342-374). MIT Press.

Xu, G., Chang, P., Ramachandran, S., Danabasoglu, G., Yeager, S., Small, J., ... Wu, L. (2022). Impacts of model horizontal resolution on mean sea-surface temperature biases in the community earth system model. *Journal of Geophysical Research: Oceans*, e2022JC019065. doi: 10.1029/2022JC019065

Xu, Y., & Fu, L.-L. (2011). Global variability of the wavenumber spectrum of oceanic mesoscale turbulence. *Journal of Physical Oceanography*, *41*(4), 802–809. doi: https://doi.org/10.1175/2010JPO4558.1

Xu, Y., & Fu, L.-L. (2012). The effects of altimeter instrument noise on the estimation of the wavenumber spectrum of sea surface height. *Journal of Physical Oceanography*, *42*(12), 2229–2233. doi: 10.1175/JPO-D-12-0106.1

Yarom, E., Vardi, Y., & Sharon, E. (2013). Experimental quantification of inverse energy cascade in deep rotating turbulence. *Physics of Fluids*, *25*(8), 085105. doi: 10.1063/1.4817666

Yassin, H., & Griffies, S. M. (2022). Surface quasigeostrophic turbulence in variable stratification. *Journal of Physical Oceanography*, *52*(12), 2995–3013. doi: 10.1175/JPO-D-22-0040.1

Young, W. (2010). Dynamic Enthalpy, Conservative Temperature, and the Seawater Boussinesq Approximation. *Journal of Physical Oceanography*, *40*, 394-400. doi: 10.1175/2009JPO4294.1

Young, W. (2012). An exact thickness-weighted average formulation of the Boussinesq equations. *Journal of Physical Oceanography*, *42*, 692-707. doi: 10.1175/JPO-D-11-0102.1

Zhao, M., Ponte, R. M., Penduff, T., Close, S., Llovel, W., & Molines, J.-M. (2021). Imprints of ocean chaotic intrinsic variability on bottom pressure and implications for data and model analyses. *Geophysical Research Letters*, *48*(24), e2021GL096341. doi: 10.1029/2021GL096341

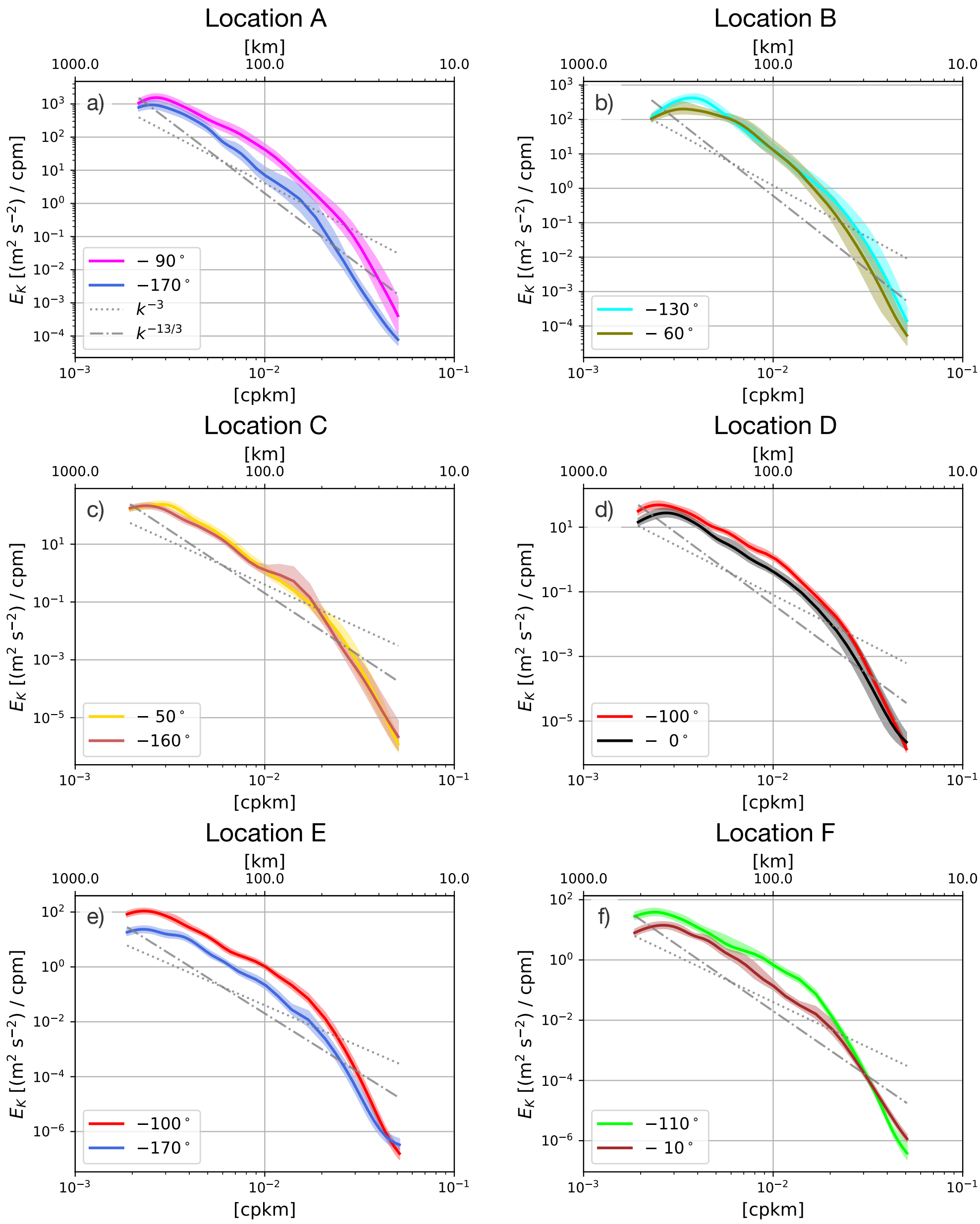

Figure 6. KE spectra $\widetilde{E}_K(\phi, k)$ plotted along the orientation of maximum and minimum energy from $z = -452$ m at all six locations (A-F) on January 1, 1967. The angles, associated with the maximum and minimum energy at each location, are color coded. The land cells are not interpolated over and data are not windowed prior to taking the wavelet transforms, differing from Fig. 3a. The 95% bootstrap confidence intervals are shown in colored shadings. Power laws with the slope of -3 and $-13/3$ are indicated with the grey dotted and dotted-dashed curves respectively.

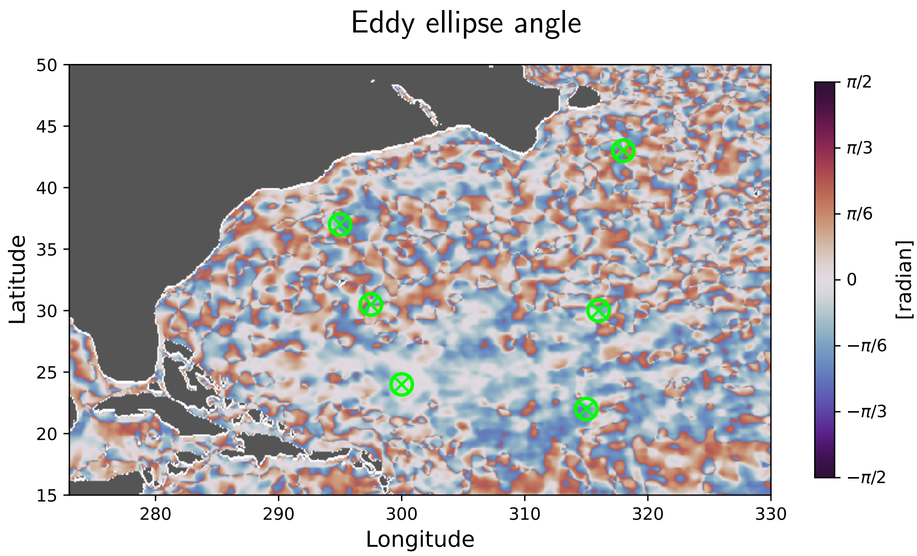

Figure 7. The eddy ellipse angle ϑ at $z = -452\,\mathrm{m}$ on January 1, 1967. The lime-colored $\otimes$ indicate locations A–F.

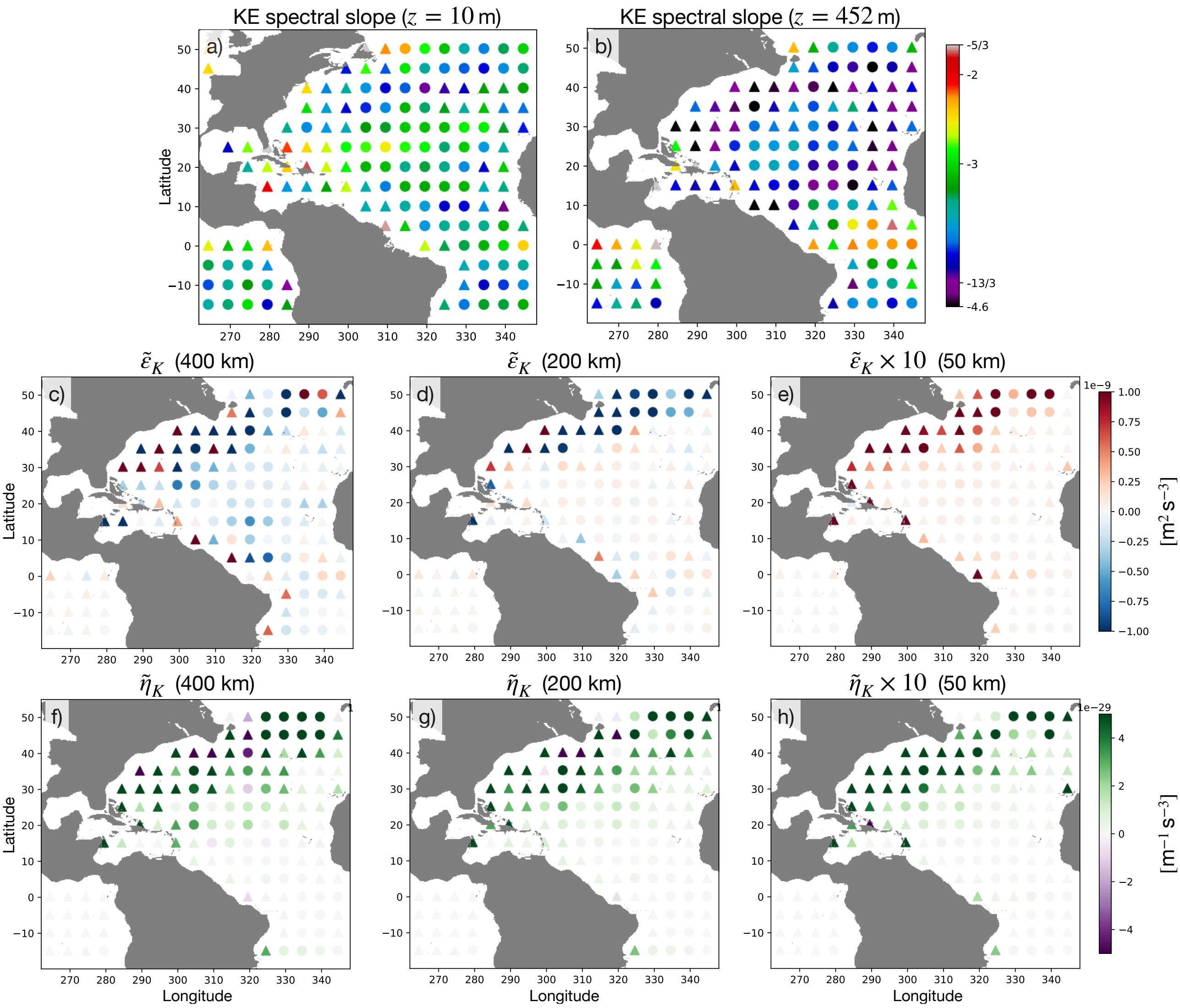

Figure 8. A map showing the slopes of KE power spectra at depths of 10 and 452 m, and spectral flux of KE ($\tilde{\varepsilon}_K$) and enstrophy ($\tilde{\eta}_K$) about the length scales of 400, 200 and 50 km at the depth of 452 m. The North Atlantic domain is configured to be zonally re-entrant. Locations with less than 30% of land cells within the 10° × 10° domain centered around each marker are shown. Locations where the 10° × 10° domain includes no land cells are shown with the circle marker and triangle marker otherwise. Land cells are not interpolated over prior to taking the wavelet transforms. The spectral flux corresponding to 50 km is multiplied by 10 to plot against the same color range.

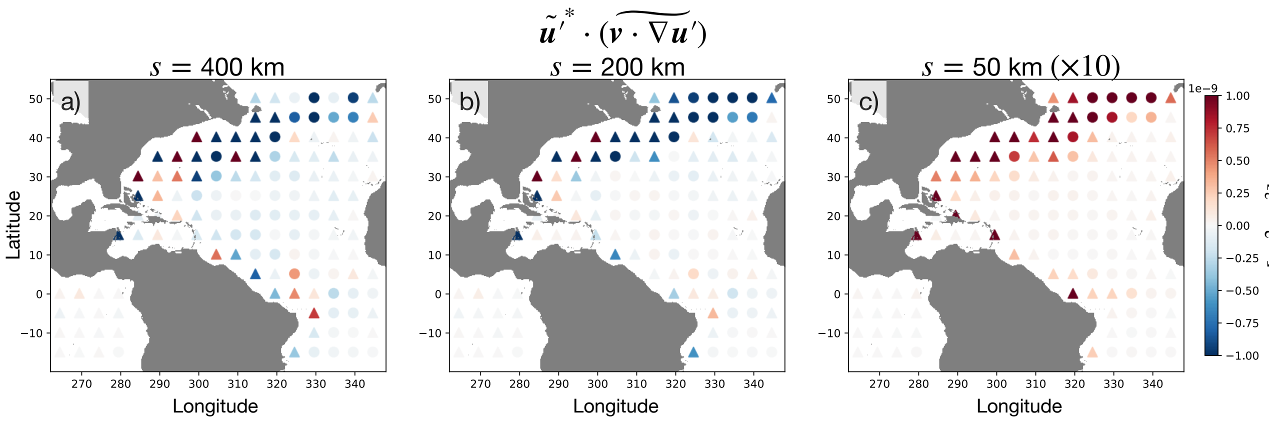

Figure 9. A map showing a part of the KE spectral flux $(-C_{\Xi}{}^{-1} \int_{k>\kappa} \langle \tilde{\boldsymbol{u}}'^{*} \cdot (\widetilde{\boldsymbol{v} \cdot \nabla \boldsymbol{u}'}) \rangle x_0^2 \kappa \, d\kappa)$ about the length scales of 400, 200 and 50 km at the depth of 452 m. Locations with less than 30% of land cells within the 10° × 10° domain centered around each marker are shown. Locations where the 10° × 10° domain includes no land cells are shown with the circle marker and triangle marker otherwise. The spectral flux corresponding to 50 km is multiplied by 10 to plot against the same color range.